Version of Record: https://www.sciencedirect.com/science/article/pii/S0169809519307410
Manuscript_59b047e2b384604b828861441a4ec024

Raindrop Size Distribution and Microphysical Characteristics of a Great Rainstorm in 2016 in Beijing, China

Li Luo[a,b] , Hui Xiao[a,b,**], Huiling Yang[a] , Haonan Chen[c,d] , Jia Guo[e], Yue Sun[a,b], Liang Feng[a,b]

[a] *Key Laboratory of Cloud-Precipitation Physics and Severe Storms(LACS),&Center of Disaster Reduction, Institute of Atmospheric Physics, Chinese Academy of Sciences, Beijing 100029, China*

[b] *University of Chinese Academy of Sciences (UCAS), Beijing 100049, China*

[c] *Cooperative Institute for Research in the Atmosphere, Colorado State University, Fort Collins, CO 80523,USA*

[d] *NOAA/Earth System Research Laboratory, Boulder, CO 80305, USA*

[e] *Beijing Metstar Radar CO.,LTD, Beijing 100085,China*

ABSTRACT

This paper analyzes the characteristics of rain drop size distributions (DSDs) and vertical profiles of hydrometeors for a severe rainstorm event that occurred in Beijing, northern China, from 19 to 21 July 2016 using *in situ* measurements from two disdrometers (OTT-Parsivel^2 and 2D-Video-Distrometer) and remote sensing data collected by a second-generation Micro Rain Radar (MRR^2). This rainstorm was characterized by stratiform precipitation with embedded strong convection on 19 July and widespread, intense mixed convective-stratified rainfall resulting in persistent rainfall between 20 and 21 July. The temporal and spatial variations in rainfall rate R, liquid water content W, reflectivity Z, DSDs and the gamma DSD parameters in different precipitation episodes of this event are derived and compared between two meteorological stations in Beijing.

Rainfall throughout the entire event was characterized by large concentrations of small- to medium-sized raindrops (diameters between 2 and 4 mm) and few larger particles (D>4 mm), resulting in small values of reflectivity Z (<40 dBZ) and liquid water content W (<1.0 g m^{-3}). In addition, the $\log_{10}N_w$-D_m scatter pairs recorded during the convective phase of this rainstorm indicate maritime-like convection. The time evolution of DSDs shows that most single peak DSDs occurred during stratiform rainfall, and bimodal DSDs were observed when the convective rainfall cells passed by and collisional breakups occurred. The gamma DSD model with a single peak in the stratiform phase of the storm and the bimodal DSD in the convective episode of the storm are quantitatively evaluated. In addition, in each precipitation episode, the differences in exponent b and coefficient A of the Z-R relationship between the two stations are smaller for stratiform rainfall than for convective rainfall due to the more evident variability of drop size and number concentration in convective rain. The physical nature of this relationship and the possible mechanisms leading to diverse characteristics in different phases of this heavy rainstorm are discussed.

Keywords: great rainstorm; northern China; raindrop size distribution; precipitation microphysics; Z-R relation.

1. Introduction

Strong convective clouds usually cause heavy precipitation, hailstones, lightning strokes, downbursts and even tornadoes. They are often organized into strong convective weather systems, such as thunderstorms, squall lines and rainstorms, which are very abrupt and destructive. The direct economic losses caused by torrential rainfall from 2008 through 2013 in China ranged from $14.3 million to more than $8.6 billion, with an annual damage of approximately $1.6 billion (Min et al., 2016). Southern China and the Yangtze River Basin are traditionally rainstorm-prone areas. However, the frequency of heavy precipitation with abrupt onset and strong rain intensity has gradually increased

in northern China in recent years (Zhao et al., 2018). During 19-21 July 2016, an extraordinary rainstorm with local rainfall amounts of 449 mm (Yang et al., 2018), fell over northern China, including Beijing City and its adjacent regions. The most intense, widespread, and persistent rainfall occurred on 20 July, causing severely localized urban flash floods, so this extreme rainfall event is referred to as the "7.20" extreme rainstorm hereafter. This event was another extreme rainstorm in northern China following "7.21" Beijing extraordinary rainstorm occurred in 2012 (Guo et al., 2015).

Although large-scale weather models have shown some improvements in the spatial and temporal distributions of precipitation over the past few years (Beate and Michael 2012; Lopez, 2007), extreme rainfall events are still difficult to forecast since the weather patterns and atmospheric processes in one region generally cannot represent those in other regions (Boucher et al., 2013; Friedrich et al., 2016). The development of remote sensing (e.g., radar) and *in situ* observational instruments provides a good opportunity to improve rainfall monitoring and nowcasting. In addition, high-resolution microphysical observations can be used to evaluate model performance (Stephens et al., 2010) and improve microphysical schemes of weather forecasting model (Jakob, 2010).

Raindrops are the product of the interaction of macro- and microphysical processes in clouds, and the variations in DSDs are related to the dynamic, thermal and microphysical mechanisms of precipitation formation and evolution (Mason, 1954). The characteristics of DSDs and their vertical evolutions can be obtained by ground-based disdrometer and radar remote sensing observations. A detailed knowledge of the variations in DSDs is helpful in understanding the microphysical characteristics of precipitation (liquid water content, raindrop size distribution, etc.) and is also of great importance for radar quantitative precipitation estimation (QPE) (Chen et al., 2017; Gou et al.,2018) and microphysical parameterization in numerical weather prediction models (Tao et al., 2014).

Previous studies on the DSDs of rainstorms over northern China are relatively rare compared to studies in southern China. Tang et al. (2014) compared and analyzed the DSD characteristics of stratiform and convective precipitation in Beijing, Zhangbei (both in northern China) and Yangjiang (in southern China) using one-year observations from a one-dimensional particle size velocity (Parsivel) disdrometer manufactured by OTT Messtechnik, Germany. These authors noted that the average DSDs of both convective and stratiform rainfall in Beijing and Yangjiang are in good agreement with gamma distributions (Ulbrich, 1983), while the averaged DSDs in Zhangbei cannot be well fitted by either gamma or exponential distributions (Marshall and Palmer, 1948). Wen et al. (2017a) investigated the statistical characteristics of summer and winter precipitation over the Northern China Plain by using a two-dimensional video disdrometer (2DVD) and a micro rain radar (MRR). They obtained a raindrop shape model in northern China for the first time. These studies mainly focused on the generally statistical characteristics of rainfall over northern China (Ji et al., 2019; Ma et al., 2019; Tang et al., 2014). Zhao et al. (2018) studied the mechanism of the "7.20" extreme rainstorm from atmospheric circulation and the characteristics of the weather system. Yang et al. (2018) investigated the spatial distribution of total rainfall over Beijing City on a larger spatial scale.

However, extensive analysis is still lacking for the microphysical processes of extreme events, such as the spatial and temporal evolution of the DSDs during different precipitation stages of the "7.20" great rainstorm. Therefore, this paper presents the detailed microphysical rainfall characteristics (i.e., rain intensity, mean diameter, liquid water content and drop number concentration) measured by two disdrometers (2DVD and Parsivel^2) deployed at two locations and a micro rain radar (MRR^2) during different periods of the "7.20" extreme rainstorm in Beijing. DSDs obtained from two disdrometers separated by a distance of 26 kilometers are compared to investigate the evolution of microphysical signatures associated with this rainstorm. In addition, the vertical variability of bulk properties of this rainstorm is documented to provide an insight into the microphysical processes of heavy rainstorms over northern China. The remainder of this paper is organized as follows. Data sources and analytical methods are presented in Section 2. The microstructural characteristics of this rainstorm observed by disdrometers and the vertical structures of rainstorm observed by MRR are detailed in Section 3. Section 4 summarizes the main findings of this study and suggests future directions for this research.

2. Data and methods

2.1. Instruments and dataset

The datasets used in this study were collected by two disdrometers (OTT-Parsivel^2 and 2DVD), two rain gauges and a second-generation vertically pointing MRR (i.e., MRR^2) from 19 to 21 July 2016. The instrument locations are illustrated in Fig. 1. The OTT-Parsivel^2 disdrometer and a rain gauge are deployed at the Institute of Atmospheric Physics (IAP), Chinese Academy of Sciences (39°59′ N, 116°23′ E). The third-generation 2DVD, the MRR^2 and a rain gauge are deployed at Shunyi National Weather Station, Beijing (hereafter referred to as SY) (40°08′ N, 116°37′ E). Here, it should be noted that disdrometers are mostly confined to fixed locations, recording time series of surface DSDs as precipitation systems pass by (Wen et al., 2017b). Therefore, we use the radar reflectivity data obtained from a scanning S-band Doppler weather radar to complement the analysis. This S-band radar, located at the observatory in the southern suburbs of Beijing, is managed by the Beijing Meteorological Bureau to monitor the relevant macro-structural evolution of severe weather events. As shown in Fig. 1, the SY site is ~26 km northeast of the IAP site, and the S-band radar is ~20 km and ~37 km south of the IAP site and the SY site, respectively.

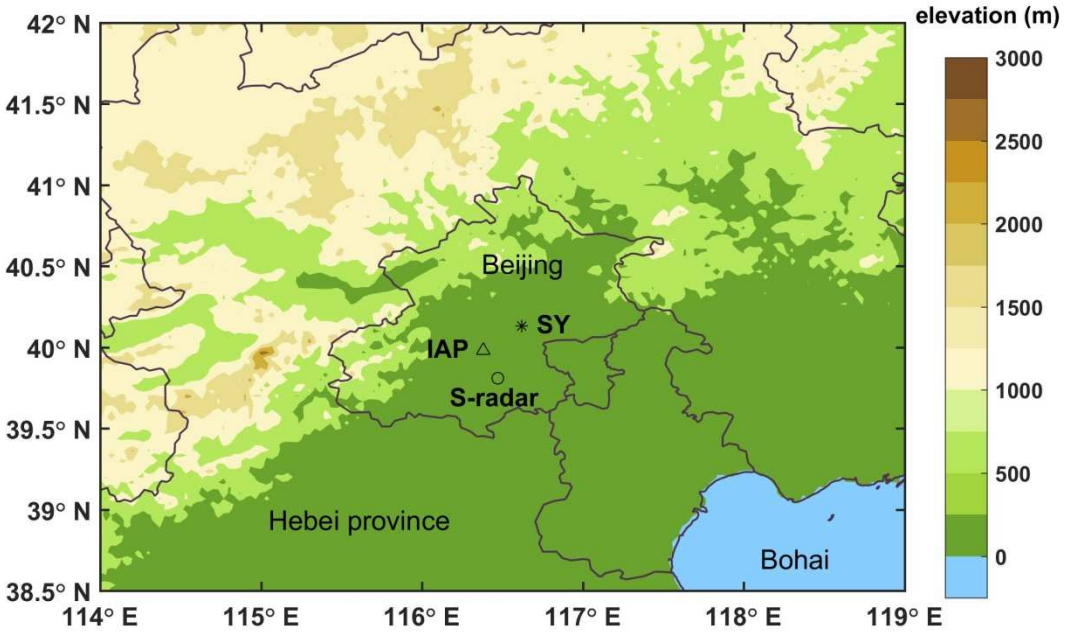

Fig.1. The geographical locations of instruments in Beijing city used in this study. The 2DVD, MRR^2 and a rain guage are located at the SY site (∗). The PARSIVEL^2 and an identical rain guage are located at the IAP site (Δ). The S-band weather radar (○), owned by the Beijing Meteorological Bureau, is ~ 26 km southeast of the IAP site and ~37 km southwest of the SY site.

The OTT Parsivel^2 located at the IAP site is an advanced optical disdrometer that uses a laser diode to produce a horizontal sheet of light 30 mm wide and 180 mm long. The particle size is estimated from the decrease in magnitude of the voltage when the particles pass through the laser beam, while the drop fall velocity is estimated from the duration of the decrease in the intensity of light, assuming that the particle is spherical [Figure 1 in Löffler-Mang and Joss, (2000)]. Because the signal-to-noise ratio (SNR) of each raindrop is small in the two minimum size ranges, there are no particles recorded for the first two bins and the minimum detectable particle size is approximately 0.312 mm. Parsivel^2 has been widely used due to its stable measurement performance, precise waterproof design and easy operation (Löffler-Mang and Joss, 2000).

The 2DVD installed at the SY station uses two orthogonal cameras to take high-speed pictures of particles, measure the shadows of precipitation particles and reconstruct their shapes, sizes and falling velocities (Kruger and Krajewski, 2002). The performance of the 2DVD has been evaluated and improved since its invention. The effect of raindrop splashing on the observation area and the error caused by strong winds and turbulence can be effectively reduced in the third-generation 2DVD (Nešpor et al., 2000; Tokay et al., 2013), which is used in this study.

The micro rain radar (MRR^2) is a vertically pointing, low-cost, frequency-modulated continuous

wave (FM-CW) Doppler radar operating at 24.1 GHz (Peters et al., 2002). Its transmitting power is only 50 mW, which avoids the separation of transmitting and receiving antennas (Peters et al., 2005). The DSDs can be derived from the received Doppler spectra under the hypothesis of the relation between particle diameter and velocity proposed by Atlas et al. (1973). More details about the DSD retrieval procedures can be found in (Löffler-Mang et al., 1999; Peters et al., 2005). After obtaining the DSDs, the vertical profiles of radar reflectivity, rain rate and liquid water content can be calculated. The maximum height that can be detected by MRR^2 is from 300 m to 6000 m and there are 30 layers of range gates; each layer can be configured with a resolution of 10-200 m according to actual needs (the vertical resolution is 100 m in this study). The sizes of the particle retrieved from MRR^2 are between 0.246 and 5.03 mm, corresponding to velocities of 0.78~9.34 m s^{-1} (Peters et al., 2005). In this study, MRR^2 data have been calibrated to reduce systematic errors following Wen et al. (2017a), and the first two range gates are excluded according to the guidance provided in the METEK manual since the first two bins are vulnerable to near-field effects. The 300 m height is considered the ground approximation. The ground level results showed good correlations with the 2DVD measurements [see Fig.1 in Wen et al. (2017a)].

In addition, two capacitive rain gauges (RG) are used to collect hourly rainfall accumulation, which serve as the ground truth. The gauges are configured with 0.1-mm resolution and 1-min time resolution.

2.2. Observation errors and disdrometer data quality control

Previous studies (Krajewski et al., 2006; Nešpor et al., 2000; Tokay et al., 2013) have identified various error sources that affect the data quality of ground-based disdrometers (2DVD or Parsivel^2), such as instrument background noise, mixed phase precipitation, strong winds, turbulence, edge effects, and splashes of raindrops on the housing of the instrument. This paper uses a quality control method based on the particle size versus velocity matrix, which can eliminate errors such as raindrop spatter caused by the edge effect of the sampling area, strong wind and/or heavy precipitation effect. This algorithm has been utilized and verified in many studies (Friedrich et al., 2013a; Jaffrain and Berne, 2011; Kruger and Krajewski, 2002; Thurai and Bringi, 2005; Wen et al., 2018):

$$\left| V_{measured} - V_{ideal} \right| < cV_{ideal} \quad (1)$$

where $V_{measured}$ is the measured fall velocity and V_{ideal} is the fall velocity derived from the equation given by Brandes et al. (2002). Previous research (e.g., Chang et al., 2009; Kruger and Krajewski, 2002; Thurai and Bringi, 2005; Tokay et al., 2001) recommended a c value of 0.4 for the 2DVD observations. Other studies (Friedrich et al., 2013b; Jaffrain and Berne, 2011) used a threshold of 60% above or below the fall velocity-diameter relationship to remove misclassified drops observed by Parsivel^2. In this study, the coefficient c is set to 0.6 to conservatively remove the outliers for both disdrometers.

Using this velocity-based filter is not expected to affect the drop shapes or the mean velocity, despite the fact that it modifies the drop size distribution for very small drops. Fig. 2 shows the two limits superimposed on the number of drops observed by Parsivel^2 (the left panel) and 2DVD (the right panel) on a velocity-diameter plot. For only comparisons of the counts of particles measured by the two instruments in the same diameter-velocity space, 2DVD data are processed using 32 Parsivel^2 diameter bins. Here, it should be noted that the velocity-based filter is applied to each raindrop recorded by 2DVD. As shown in Fig. 2, more large raindrops (D>4 mm) with fall velocities less than 2 m s^{-1} are observed by Parsivel^2, while more small and medium-sized (D<4 mm) drops with high velocities (V>10 m s^{-1}) are measured by 2DVD. Instruments used under strong wind conditions (wind speed > 10 m s^{-1}) may measure a large number concentration of raindrops with large diameters (>5 mm) and unrealistically slow fall velocities (<1-2 m s^{-1}) due to the misclassification of particles (Friedrich et al., 2016). If the particles fall on the edge of the sampling area, they may break into smaller drops, resulting in many small particles falling faster than normal hydrometeor particles (Illingworth et al., 1987; Nešpor et al., 2000; Schuur et al., 2001; Sevruk, 1982; Yuter et al., 2006). Fig. 2 shows that the main source of error in Parsivel^2 observations is from strong wind, while the errors in 2DVD data are mainly from the splashing effects of raindrops and drops that fall in the margins, leading to many smaller drops with higher fall speeds (Fig. 2b).

After quality control, the errors mentioned above can be substantially eliminated. In total, approximately 26% and 33% of raindrops from the Parsivel^2 and 2DVD are eliminated, respectively. Then, the remaining data from the two disdrometers are fitted by quartic polynomial functions:

$$V_{PAR} = 0.3175 + 3.3554D - 0.376D^2 + 0.0008D^3 - 0.0013D^4 \quad (2)$$

$$V_{2DVD} = -1.1259 + 7.1755D - 2.0296D^2 + 0.2660D^3 - 0.0119D^4 \quad (3)$$

where D (mm) is the equivalent volume raindrop diameter. The judging coefficients of the fitting equations (coefficients of determination) are all greater than 0.99, indicating that the average falling velocities measured by the two instruments are in good agreement with the falling velocities derived from the empirical equations, demonstrating the effectiveness of the filter method and the reliability of the observations from the two types of disdrometers.

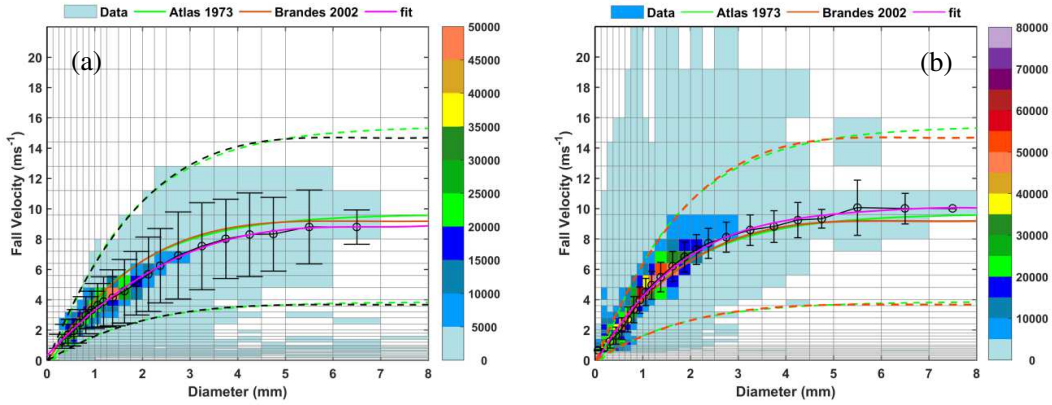

Fig.2. Fall velocity-diameter histograms observed by (a) Parsivel^2 and (b) 2DVD. The color density indicates the number of drops (raw counts) in the corresponding diameter bin and velocity interval accumulated over the whole event. The magenta solid line is the polynomial fitting curve, the orange solid line indicates the drop terminal velocity from Brandes et al. (2002), the green solid line indicates the empirical fall velocity–diameter relation for rain described in Atlas et al. (1973) and the two dashed lines represent the ±60% filter of raindrops.

During the whole precipitation event, 2DVD and Parsivel^2 collected 2,724 and 3,922 1-minute samples, respectively, which are used to calculate hourly rainfall and compared with observations at each adjacent rain gauge, as shown in Fig. 3. We can see that high consistency is shown between the disdrometer and the rain gauge; the two correlation coefficients (CC) are both higher than 0.99, and the standard deviations (STD) are both less than 0.2 mm, except for the root mean square error (RMSE), which is slightly higher at the SY site. In other words, the two instruments are highly accurate in detecting hourly rainfall over the entire period of this precipitation.

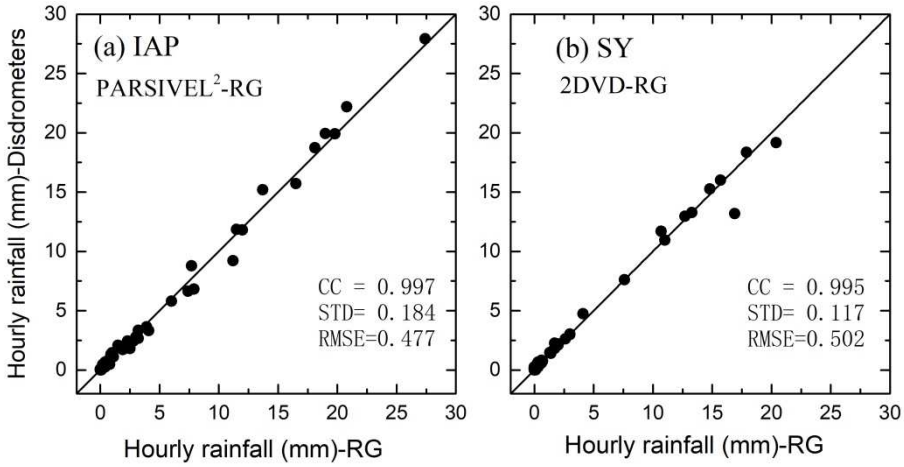

Fig.3. Comparisons of hourly rainfall (in units of mm) between **(a)** Parsivel and rain gauge and **(b)** 2DVD and rain gauge. CC, STD (mm) and RMSE represent the correlation coefficient, standard deviation and root mean square error, respectively.

2.3. Raindrop size distribution

According to the different measuring principles of 2DVD and Parsivel[2], the number concentration of raindrops ($N(D_i)$: m^{-3} mm^{-1}) per unit volume per unit size interval at a discrete instant are calculated using the following equations:

$$N(D_i)_{2\mathrm{DVD}} = \frac{1}{\Delta t \Delta D}\sum_{j=1}^{m_i}\frac{1}{A_j \mathrm{V}_j} \tag{4}$$

$$N(D_i)_{\mathrm{PARSIVEL}} = \frac{1}{\Delta t}\sum_{j=1}^{32}\frac{n_{ij}}{A\mathrm{V}_j \Delta D_i} \tag{5}$$

where Δt in Eqs. (4) and (5) is the time interval (60 *s* is used in this study). In Eq. (4), i is the size index; j is the particle index; A_j (mm^2) and V_j (m s^{-1}) are the sensing area and fall velocity for drop j, respectively; and m_i is the number of drops within size class i and time interval Δt. ΔD (mm) represents size-sorted categories of equivalent-volume diameters, and 0.2 mm is used. In Eq. (5), n_{ij} is the number of drops within size bin i and velocity bin j, A is the sampling area (54×10^{-4} m^2), V_j (m s^{-1}) is the fall speed for the velocity bin j, and ΔD_i (mm) is the corresponding diameter interval.

After the raindrop size distribution is obtained, the rainfall integral parameters such as rainfall rate R (mm h^{-1}), liquid water content W (g m^{-3}), radar reflectivity Z (mm^6 m^{-3}), and the total number concentration of raindrops N_t (m^{-3}) can be derived as follows:

$$R = \frac{6\pi}{10^4}\sum_{i=1}^{L} D_i^3 \mathrm{V}_i N(D_i)\Delta D_i \tag{6}$$

$$W = \frac{\pi}{6000}\sum_{i=1}^{L} D_i^3 N(D_i)\Delta D_i \tag{7}$$

$$\mathrm{Z} = \sum_{i=1}^{L} D_i^6 N(D_i)\Delta D_i \tag{8}$$

$$N_t = \sum_{i=1}^{L} N(D_i)\Delta D_i \tag{9}$$

where L is the total number of bins, D_i (mm) is the equivalent volume diameter of raindrops for size bin i, ΔD_i (mm) is the corresponding diameter interval and V_i (m s^{-1}) is the fall speed for the velocity bin i. The equivalent volume diameters are sorted into size categories of 0.2 mm only for 2DVD. The n-th moment expression of DSD is as follows:

$$M_n = \int_0^{\infty} D^n N(D) dD \tag{10}$$

The mass weighted mean diameter D_m is the ratio of the 4th moment to the 3rd moment:

$$D_m = \frac{M_4}{M_3} \tag{11}$$

The normalized truncation parameter N_w (m^{-3} mm^{-1}) is defined as:

$$N_w = \frac{4^4}{\pi\rho_w}\left(\frac{10^3 W}{D_m^4}\right) \tag{12}$$

where ρ_w is the density of water (1.0 g cm^{-3}).

In this study, we use the well-known gamma function to represent the DSD model (Ulbrich, 1983)

$$N(D) = N_0 D^{\mu} \mathrm{e}^{-\Lambda D} \tag{13}$$

where D (mm) is the equivalent volume diameter of raindrops; N_0 ($mm^{-1-\mu}$ m^{-3}) is the intercept parameter; μ (dimensionless) is the shape parameter and Λ (mm^{-1}) is the slope parameter. When $\mu > 0$, the DSD curve has a convex shape, whereas when $\mu < 0$, the shape is a concave.

3. Results and discussions

3.1. Synoptic environment and case description

Due to the combined effects of the Huang-Huai cyclone in central China and the southwest vortex in southwestern China, a large area of heavy rainstorms occurred in northern China from 19 to 21 July 2016. The general trend of this precipitation system was moving from southwest to northeast and it remained over Beijing City and its adjacent areas for a long time (Zhao et al., 2018). The synoptic situation of this precipitation system was analyzed using the National Centers for Environmental Predication's (NCEP) final operational global analysis data (FNL) on 1°×1° grids (see Figs. 4a-b) at 02:00 LST 19 July. Fig. 4c shows the stratification curve and convective available potential energy (CAPE) for Beijing based on the sounding data at Beijing station (No. 54511, from the University of Wyoming: http://weather.uwyo.edu/upperair/sounding.html). Almost the entire region of northern China was influenced by the positive vorticity at a height of 500 hPa. A closed vortex, with a center value of ~5760 gpm, appeared over the southwest side of the Tai-Hang Mountains (approximately 35-40° N, 113-114° E in Fig. 4a). At the same time, there was a closed low pressure center at the level of 850 hPa (Fig. 4b), and the high-level divergence and low-level convergence yielded enhanced updrafts and promoted the occurrence, development and maintenance of cyclones. Moreover, the relative humidity in northern China was more than 70% (Fig. 4b) due to the moist airflow from the Bohai Sea southeast of Beijing, causing moist conditional instability and creating a very favorable environment for the development of this rainstorm (Zhao et al., 2018).

Fig. 4c also reports the sounding curve at 08:00 LST 19 July at Beijing station. The wind veered from easterly near the ground to southerly at low levels then became westerly at high levels, indicating warm moist air advection in the atmospheric boundary layer. The CAPE was more than 755.1 J kg^{-1}, resulting in favorable atmospheric conditions for convection development (Weisman et al., 1988). The lifting condensation level (LCL) was approximately 0.4 km above the sea level, and the melting level (0°C, ~ 5 km) favored the warm rain processes (Petersen and Rutledge, 2001).

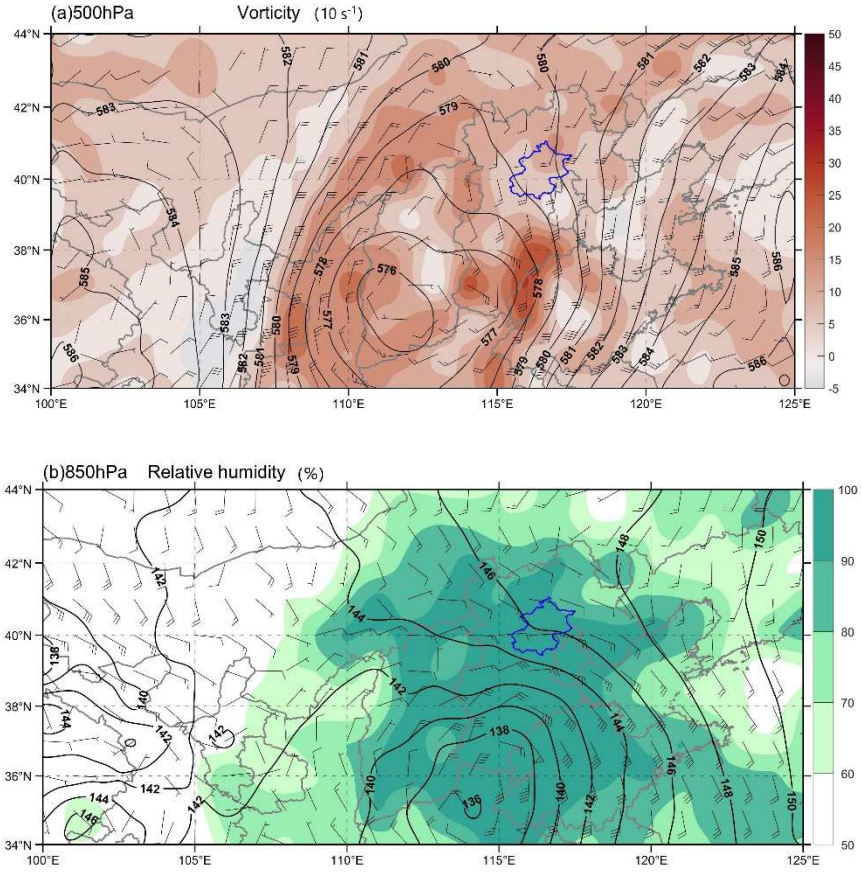

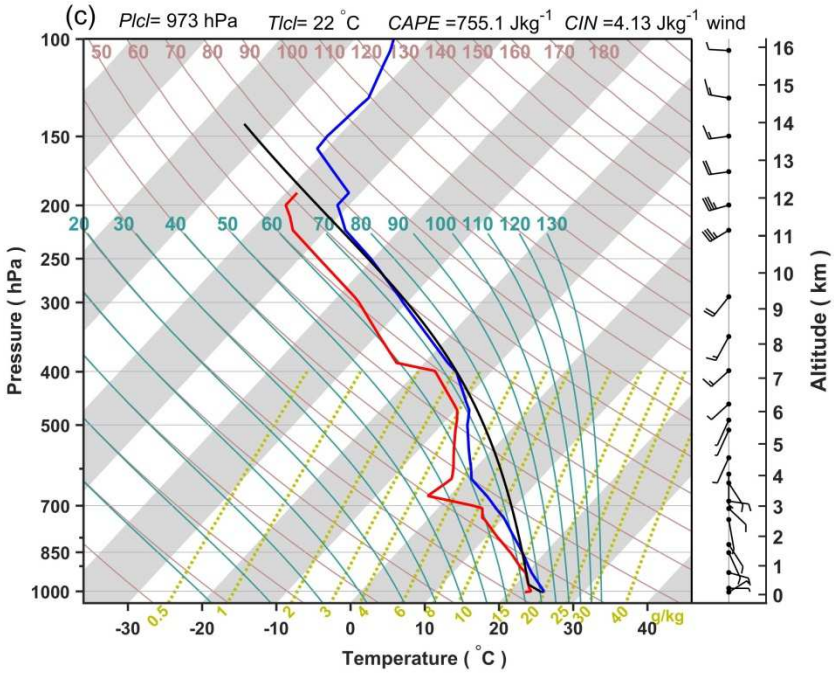

Fig.4. Contour plots of (a) vorticity (10 s^{-1}) at the 500-hPa level and (b) relative humidity (%) at the 850-hPa level in the early stage of this heavy rainfall (02:00 LST 19 July) and (c) the skew *T*-log*P* sounding profiles from the Beijing weather station at 08:00 LST 19 July, 2016. The data used in Fig. 4a and Fig. 4b are from the National Centers for Environmental Predication's (NCEP) Final (FNL) 1°×1° analysis at 02:00 LST 19 July. The black contour lines in Fig. 4a and Fig. 4b represent the geopotential height (in dagpm, i.e., 10 geopotential meters). The blue border is the city boundary of Beijing. The blue, black and red solid lines in Fig. 4c represent the stratification curve, temperature profile and dew point profile, respectively.

Fig. 5 presents the constant altitude plan position indicator (CAPPI) scans of reflectivity at a 1-km height from an S-band weather radar (S-radar) with a 200-km range. The precipitation lasted approximately 3 days from 19 to 21 July. The precipitation process can be divided into two rainfall episodes. At the beginning, a widespread stratiform rain band with strong embedded linear convection cells developed on the morning of 19 July 2016 over the southern part of northern China and gradually moved counterclockwise toward the north (Fig. 5a, the 1st rainfall episode). The most intense, widespread, and persistent rainfall occurred from the morning to the evening of 20 July (Figs. 5b-d). After this time, the entire rain band gradually moved out of Beijing city and entered a dissipating episode (Fig. 5e) until approximately 6:00 LST 21 July (the 2nd rainfall episode).

In terms of the rainfall duration over the SY and IAP sites in Beijing, this event can be subdivided into 5 rain stages based on the rain rate measured by surface disdrometers and the radar measurements. The 1st rainfall episode (S1), from 06:15 to 16:34 LST 19 July (Fig. 5a), was identified as a mixed convective-stratiform (CS) rainfall episode characterized by widespread, long-lasting stratified precipitation with strong embedded convection cells. From 00:24 LST 20 July, uniform stratiform-cloud precipitation was observed first at the IAP station. After approximately 1.5 hours, the SY site began to record rainfall at 01:42 LST 20 July, and both stations were covered by the wide stratified precipitation until 07:50 LST 20 July (Fig. 5b). This stratiform precipitation episode (S2) lasted approximately 8 hours. The third rainfall episode (S3), from 08:00 to 16:30 LST 20 July (Fig. 5c), was the strongest convective precipitation phase of this event. The maximum radar reflectivity reached 54 dBZ (not shown), and almost of Beijing city and its adjacent areas (~400 km from the radar) were covered by this strong precipitation phase. Starting at 17:00 LST 20 July, both stations were marginally touched by a second mixed CS rainfall stage (Fig. 5d). Station SY recorded the last rain data sample at 20:12 LST 20 July, while station IAP observed rainfall until 01:00 LST 21 July. This period was referred to as S4. Finally, with the northward movement of the rain band, some sporadic marginal rainfall passed over both sites (Fig. 5e). During this final rain episode (S5), the ending times of rainfall recording were 04:02 LST 21 July at IAP and 06:09 LST 21 July at SY, and shallow convective

precipitation (Blyth et al., 2013; Hamada et al., 2015; Thompson et al., 2015) was identified from the echo structure detected by the micro rain radar.

In the following sections, DSDs and rainfall characteristics during the five stages are extensively investigated in order to resolve the microphysical processes of this extreme rainfall event. In addition, DSDs from two sites are compared to reveal the spatial variations in rainfall characteristics.

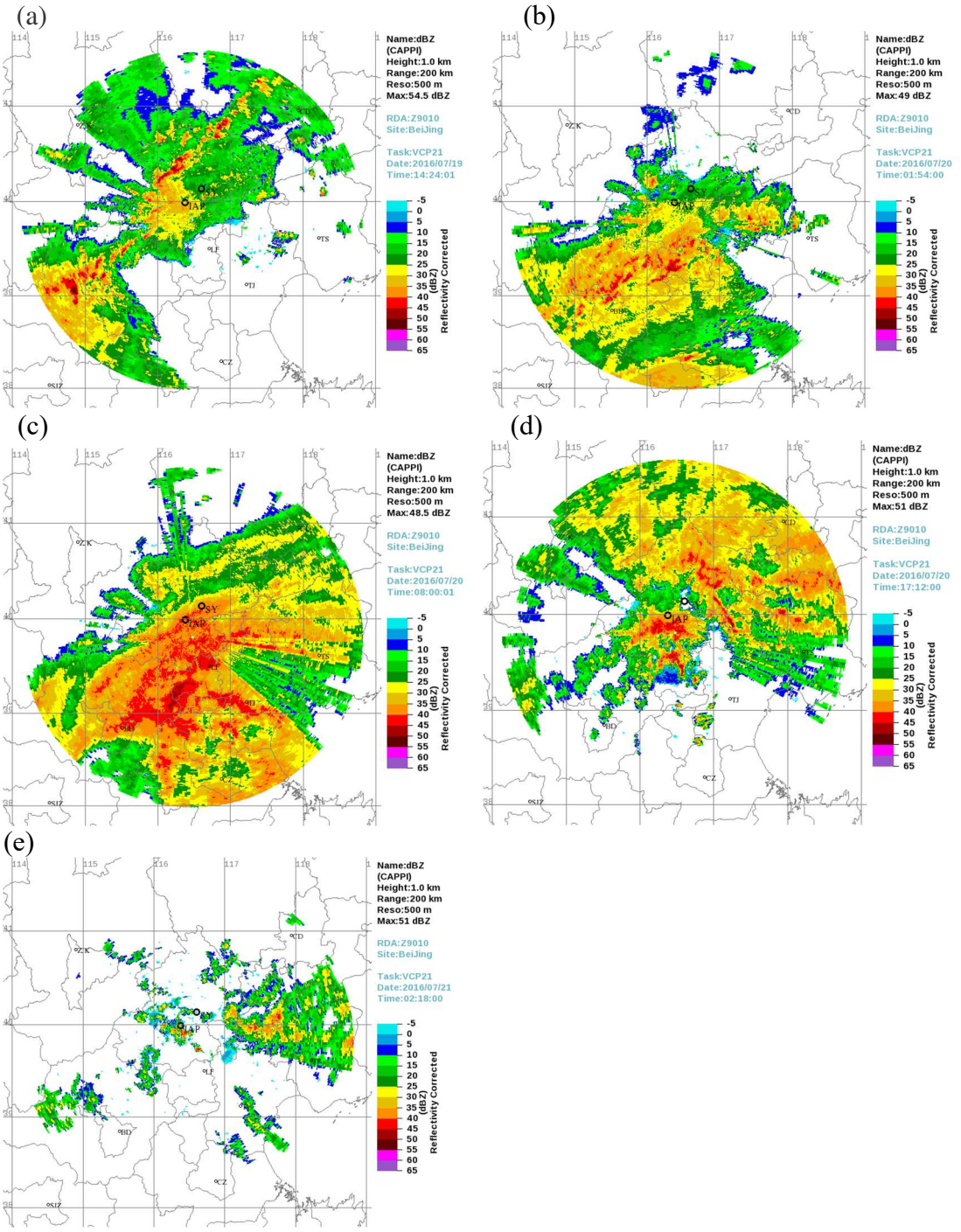

Fig.5. The constant altitude plan position indicator (CAPPI) of reflectivity (dBZ) at 1-km height with 200 km range from Beijing S-band weather radar during the five different rainfall episodes: (a) the mixed convective-stratiform (CS) rainfall echoes at 14:24 LST 19 July, (b) the stratiform rain echoes at 01:54 LST 20 July, (c) the convective rainfall echoes at 08:00 LST 20 July, (d) the second mixed CS echoes at 17:12 LST 20 July and **(e)** the shallow rain echoes at 02:18 LST 21 July 2016.

3.2. Spatial and temporal variability of rainfall characteristics

3.2.1. Spatial variations in rainfall

Fig. 6a shows the spatial distribution of the cumulative rainfall in Beijing City during the time period from 06:00 LST 19 July to 18:00 LST 21 July 2016 based on the gridded hourly precipitation data provided by the National Meteorological Information Center of China. The rainstorm affected all districts and counties of Beijing City, with an average rainfall amount of 209.1 mm during the whole event. The local minimum rainfall was 44.1 mm, which occurred in Xinchengzi town in the northeast corner of Miyun (MY) district, and the local maximum rainfall reached 356.5 mm in Wenquan village in Haidian (HD) district. Rainfall gradually decreased from southwest to northeast in the city; the area of higher rainfall (250~450 mm) accounted for approximately 1/3 of the total area of the city, and the lower rainfall (100~250 mm) area accounted for about 2/3 of the total area of the city.

The time series of hourly rainfall collected at stations IAP and SY from 06:00 LST 19 July to 06:00 LST 21 July are illustrated in Fig. 6b. The rainfall with R>2 mm h^{-1} in this rainstorm lasted for more than 13 hours. The hourly rainfall at IAP was always higher than that at SY during the period from 06:00 to 12:00 LST 20 July; then, the former was lower than the latter before 16:00 LST 20 July. The maximum hourly rainfall observed at the IAP site was close to 30 mm, while approximately 18.4 mm at the SY site. The maximum instantaneous rainfall rate (~75.7 mm h^{-1}) occurred at SY. In addition, the hourly rainfall derived from MRR at the 300 m level was in accordance with the results obtained by 2DVD since both are located at station SY. In general, the variation in hourly rainfall with time at station SY seemed to lag behind that at station IAP due to the northward movement of the storm.

Table 1 details the rainfall statistical characteristics collected by rain gauge (RG), 2DVD, Parsivel[2] and MRR at IAP and SY sites during the first and second episodes of the "7.20" extreme rainstorm. The cumulative rainfall collected by rain gauges at IAP and SY sites in the 1st episode was 17.1 mm and 4.0 mm, 220.3 mm and 162.9 mm in the 2nd episode, respectively. The main rainfall occurred in the 2nd episode of this rainstorm. Moreover, Table 1 also shows that a good consistency in cumulative rainfall between the disdrometers and rain gauges, while MRR has a deviation of rainfall about 10% compared with the rain gauge.

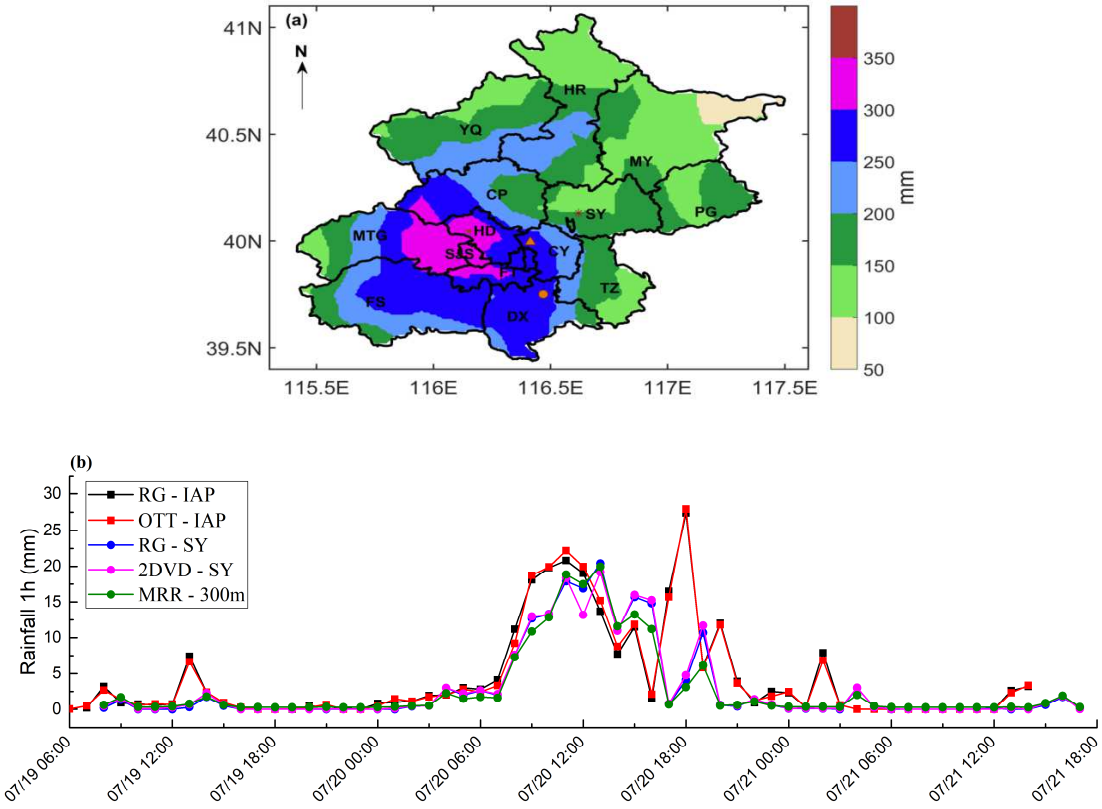

Fig.6. (a) The spatial distribution of total rainfall during the whole "7.20" rainstorm event derived from the gridded hourly precipitation data obtained from the National Meteorological Information Center of China. The capital letters in (a) represent the abbreviations of geographical names for each district in Beijing. (b) Hourly rainfall observed by 2DVD, Parsivel[2], MRR[2] and

rain gauges (RG).

Table 1 Statistical characteristics of rainfall collected by rain guage (RG), 2DVD, Parsivel and MRR at IAP and SY sites during the first and second episodes of the "7.20" heavy rainfall event

	1st episode 07:39 - 16:34 19 July					2nd episode 00:19 20 July - 06:09 21 July				
	IAP		SY			IAP		SY		
	RG	PARSIVEL	RG	2DVD	MRR	RG	PARSIVEL	RG	2DVD	MRR
No. of 1-min samples	97	514	30	335	424	938	1572	755	1372	1472
Accumulated rainfall (mm)	17.1	16.7	4.0	5.9	4.5	220.3	221.3	162.9	162	149
Mean rain rate(mm h^{-1})	1.44	1.86	0.80	1.06	0.63	8.38	8.41	6.03	7.13	6.07

3.2.2. DSDs at two observation stations

Figs. 7a and 7c show the time series of the drop size distribution ($N(D)$: m^{-3} mm^{-1}) in logarithmic scale during the passage of this rainstorm derived from the 1-min disdrometer observations at the two sites, and the corresponding rain rates are illustrated in Figs. 7b and 7d. Due to the movement direction of this rainstorm, the front edge of the rain band first reached the IAP site at 06:15 LST 19 July, with a maximum rain rate of nearly 40.0 mm h^{-1} and raindrops smaller than 4 mm (S1 in Figs. 7a-b). Moreover, the concentrations of all diameters were less than $10^{3.5}$ (3162.3) m^{-3} mm^{-1}. Approximately 2 hours later, this rainstorm passed over site SY with two peak rain rates due to maximum drop sizes close to 4 mm (S1 in Figs. 7c-d). After this time, station IAP started to observe precipitation again. At the beginning, there was moderate rainfall with an instantaneous peak rain rate reaching 19.6 mm h^{-1} at 01:01 LST 20 July (S2 in Fig. 7b) and the maximum raindrop was close to 4 mm. Approximately 40 minutes later, a uniform stratified rainfall passed over both sites. The maximum drop diameter could be as small as 3 mm, and a roughly uniformly distributed raindrop spectrum lasted approximately 8 hours during S2. With low concentrations of all diameter droplets ($N(D)<10^3$ m^{-3} mm^{-1}), the rainfall intensities at both IAP and SY were relatively low in this period, with averaged rain rates of 2.0 mm h^{-1} and 2.5 mm h^{-1}, respectively. Then, the rain rate at the two sites gradually increased with the increasing concentrations of small drops (D<2 mm) as well as the maximum drop diameter during convective rainfall (S3). The maximum rainfall rates were 60.7 mm h^{-1} at 12:14 LST 20 July observed at the IAP site and 75.7 mm h^{-1} at 13:30 LST 20 July observed at the SY site. During S4, a second mixed CS rainfall occurred over Beijing City with rare large drops >4 mm at station IAP and all drop diameters less than 4 mm at station SY (S4 in Figs. 7a and 7c), resulting in rain rate peaks of 57.9 mm h^{-1} at IAP and 48.2 mm h^{-1} at SY. During S5, shallow precipitation was observed at both sites with a DSD cluster only containing a high concentration of small drops (D<2 mm) and the echo top of radar reflectivity was 1 km lower than the 0°C isotherm from MRR[2] (not shown), which is referred to as shallow rain as documented in Wen et al. (2016).

In general, DSDs at the two sites exhibited some similar behaviors, particularly in stratiform rainfall during S1 and S2 with maximum drop diameters less than 4 mm and number concentrations of raindrops in all diameters less than $10^{3.5}$ (3162.3) m^{-3} mm^{-1}. On the other hand, wider size spectra were shown during S3 and S4 than during stratiform rainfall. That is, convective precipitation tends to produce wide spectra resulting in a higher rain rate due to the increasing concentrations of small- to medium-sized drops. In the convective rainfall stages (S3 and S4), large concentrations of small raindrops with diameters less than 1.0 mm were recorded at both sites, but more small drops (D<0.5 mm) were observed at the SY site, and larger concentrations of small- to medium-sized drops (2-4 mm) and larger drops (D>4 mm) were observed at IAP, resulting in the accumulated rainfall for the whole 2nd episode on 20 July exceeding 200 mm (Table 1), which is similar to the results observed in tropical regions such as the Amazon of Brazil, Florida, and Kwajelein Island, where warm-rain processes are dominant (Tokay and Short 1996; Carey et al. 2001; Bringi et al. 2003; Munchak et al. 2012).

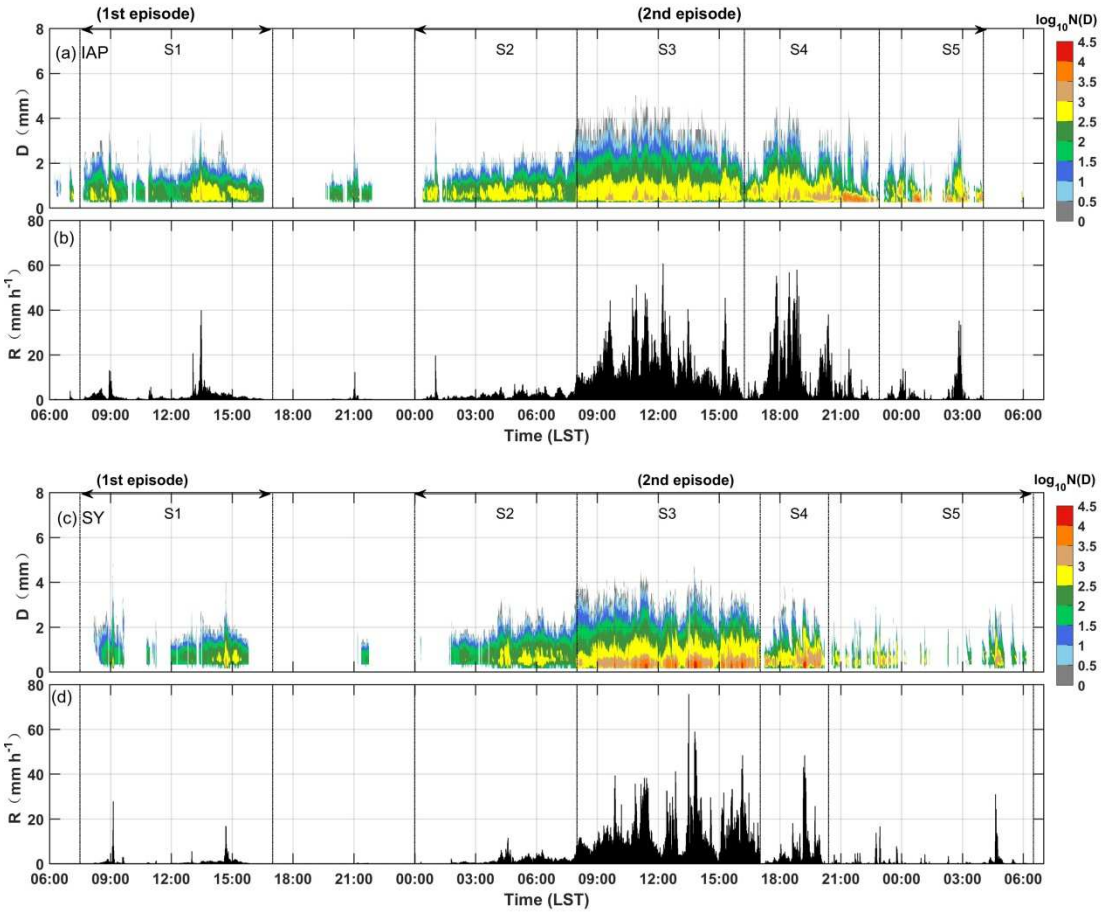

Fig.7. Time series of DSD observed by (a) the Parsivel[2] at station IAP and (c) 2DVD at station SY from 06:00 LST 19 July to 06:00 LST 21 July 2016. The color density in both (a) and (c) represents the number concentration in logarithmic units of N(D) (# m^{-3} mm^{-1}). Time series of corresponding rain rates (R: mm h^{-1}) calculated based on the 1-min DSD are shown in (b) and (d) respectively at sites IAP and SY.

3.2.3. The characteristics of bulk properties of DSDs

Fig. 8 shows the reflectivity Z (dBZ), rain rate R (mm h^{-1}), liquid water content W (g m^{-3}), median volume diameter D_0 (mm) and $\log_{10}N_w$ (N_w: m^{-3} mm^{-1}, the normalized intercept parameter), calculated from the 1-min DSDs observed by 2DVD and Parsivel[2]. In addition, these parameters at the two stations during the five different rain stages are calculated and detailed in Table 2. In general, the time variations in rainfall parameters between the two stations were similar, although the two instruments have different observation principles. Since the precipitation movement was from south to north and the SY site is ~26 km northeast of the IAP site, the variability of rainfall characteristics over time at the SY site lags relative to that at IAP site.

As shown in Fig. 8, the main features of rainfall observed at the two stations include many small raindrops with an average volume mean diameter D_0 less than 2.0 mm (Fig. 8d), and the mean values of $\log_{10}N_w$ for the two sites were 3.51 and 3.57 (Table 2). Reflectivity, liquid water content and, rainfall rate at the IAP site (the SY site), ranged on average between 31.0 and 43.0 dBZ (26.7 and 40.0 dBZ), 0.16 and 0.84 g m^{-3} (0.09 and 0.69 g m^{-3}), 1.5 and 15.7 mm h^{-1} (2.4 and 14.1 mm h^{-1}), respectively (Table 2). The D_0 values at the two stations were almost equal (Fig. 8d), but the $\log_{10}N_w$ at SY was lower during the whole precipitation process (Fig. 8e), resulting in a higher average rain rate, average water content and reflectivity at IAP (Table 2). Compared to SY observations, higher $\log_{10}N_w$ and D_0 were observed at IAP during S1, S2 and S5, along with higher reflectivity. Overall, the number concentration, median volume diameter, water content, rain rate and reflectivity are significantly higher for convective rain than for stratiform rain. It seems clear that the variations in rain rate, water content and reflectivity are mainly controlled by the size of raindrops because of the nearly unchanged $\log_{10}N_w$

before 21:00 LST 20 July. After this time, the rainfall characteristics presented variations in both drop size and number density, implying mixed control drop spectra (Steiner et al., 2004). In addition, at the beginning (S1) and ending (S5) stages of the precipitation, the values of D_0 and $\log_{10}N_w$ showed substantial fluctuations induced by the sporadic rainfall cells passing over the observation stations.

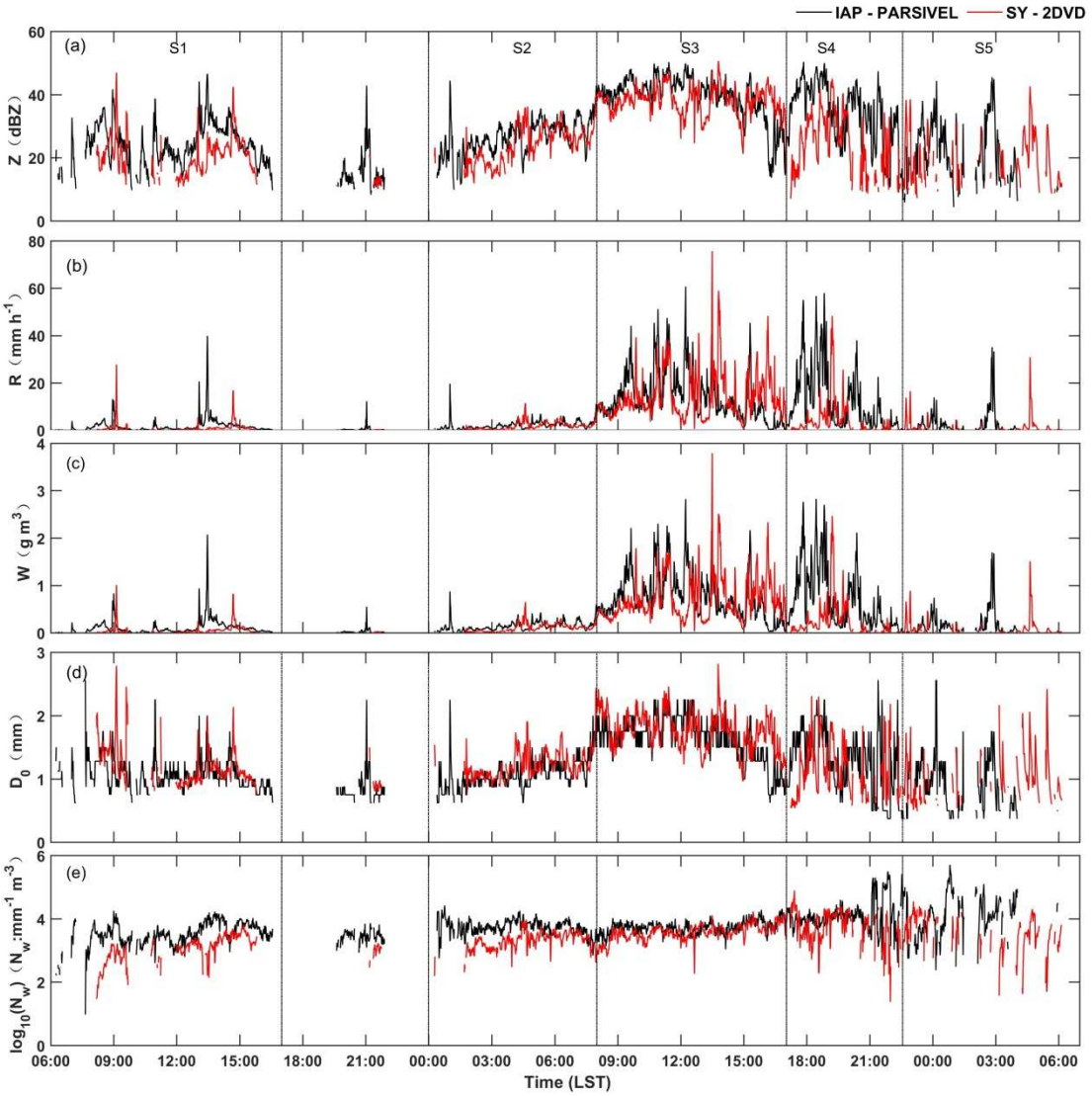

Fig.8. Surface observations from 06:00 LST 19 July to 06:00 LST 21 July 2016: (a) reflectivity Z (dBZ), (b) rain rate R (mm h^{-1}), (c) liquid water content W (g m^{-3}), (d) median volume diameter D_0 (mm), and (e) the normalized intercept parameter N_w ($m^{-3}mm^{-1}$). Data are based on disdrometer observations at stations IAP (black lines) and SY (red lines).

Table 2 Mean values of rainfall parameters (N_w: normalized DSD intercept parameter, D_0: median volume diameter, R: rain rate, W: liquid water content and Z: reflectivity) derived from composite DSDs in the five rain stages and the total samples at the two sites.

Rain stages	sites	$\log_{10}N_w$ (N_w: m^{-3} mm^{-1})	D_0 (mm)	R (mm h^{-1})	W (g m^{-3})	Z (dBZ)
S1	IAP	3.50	1.18	1.58	0.10	29.34
	SY	3.29	1.13	1.06	0.06	27.67
S2	IAP	3.72	1.17	1.96	0.14	29.43
	SY	3.55	1.16	1.77	0.10	27.77

S3	IAP	3.68	1.90	15.74	0.84	42.95
	SY	3.88	1.60	14.09	0.69	39.98
S4	IAP	4.03	1.49	13.81	0.78	41.17
	SY	4.11	1.14	6.40	0.37	34.18
S5	IAP	4.06	1.00	2.40	0.16	31.02
	SY	3.74	0.94	1.45	0.09	26.72
ALL	IAP	3.76	1.31	6.38	0.37	38.04
	SY	3.67	1.20	5.58	0.29	35.46

3.2.4. Gamma and DSD parameters derived from measurements at two stations

Fig. 9 shows scatter plots of the shape parameter μ (dimensionless), the slope parameter Λ (mm^{-1}), the mass-weighted mean diameter D_m (mm) and the logarithmic normalized intercept parameter $\log_{10}N_w$ (N_w: m^{-3} mm^{-1}) versus rainfall rate R (mm h^{-1}). The probability density functions (PDFs) of the four parameters are also illustrated in Figs. 9e-h. Note that the estimations of μ and Λ are based on the truncated moment method described in Vivekanandan et al. (2004), while D_m and N_w are calculated directly from the measured DSD. As Cao et al. (2008) noted, fitting the DSD of light rain (R<5 mm h^{-1}) always yields large μ and Λ, which may raise the slope of the mean μ-Λ relation and subsequently deteriorate the DSD retrievals from polarimetric radar measurements (Zhang et al., 2001). Therefore, the values of μ and Λ are limited to rain rates R > 5 mm h^{-1} and total raindrop number counts >1000 in this study.

As shown in Figs. 9a-d, the differences in Λ between the two sites are negligible and the values of μ as well as D_m are slightly larger at the IAP site than at the SY site, while the $\log_{10}N_w$ is smaller especially when the rainfall intensity is greater than 10 mm h^{-1}. This result indicates that the raindrop size and number concentration of drops between the two stations are similar under stratiform rainfall with a lower rainfall rate. Furthermore, positive skewness of μ and Λ is observed at both sites (Figs. 9e-f) and almost all drop spectra at two sites are described by a gamma distribution with positive μ (Fig. 9a), indicating most DSDs of this rainstorm are concave downward shape. The PDFs of D_m (Fig. 9g) and IAP $\log_{10}N_w$ (Fig. 9h) are also skewed toward positive values while the SY $\log_{10}N_w$ distribution exhibits slightly negative skewness (Fig. 9h), suggesting some similarities in the variability of D_m and $\log_{10}N_w$ between SY observations and the whole dataset recorded in the Meiyu season in eastern China (Chen et al., 2013). Compare with the values for rainfall in the summer monsoon in southern China (Zhang et al., 2019), both D_m and $\log_{10}N_w$ are smaller.

The distributions of μ, Λ, D_m, and $\log_{10}N_w$ versus rain rate R are scattered when the rain rate is less than 20 mm h^{-1}. However, the range of variation gradually decreases with increasing rain rate and tends to be more uniform at higher rain rates except for D_m. The values of μ and Λ at both sites decrease with increasing rain rate and become rather stable when the rain rate is greater than 20 mm h^{-1}; μ and Λ are respectively approximately 1.9 and 3.5 at SY and 3.4 and 3.7 at IAP, respectively. On the other hand, D_m tends to increase with increasing rain rate (Fig. 9c); the exponents of the D_m-R relationships are positive while the exponents of the N_w-R relationships are nearly zero at both sites (Fig. 9d). It is worth noting that the $\log_{10}N_w$ tends to be more uniform at higher rain rates (Fig. 9d), suggesting that the DSD variability under lower rain rates may be controlled by the coordinated combination of mean drop size and number density. In contrast, when the rain rate is greater than 20 mm h^{-1}, the DSD variability during the convective rainfall phase of this storm may be controlled by variations in drop size, as documented in (Steiner et al., 2004). At high rain rates, the DSD may reach an equilibrium state where coalescence and breakup of raindrops are nearly in balance (e.g., Hu and Srivastava 1995). Under the equilibrium state, μ, Λ and $\log_{10}N_w$ are generally constant values that are independent of the rain rate, and any increase in rain intensity is mainly due to an increase in D_m.

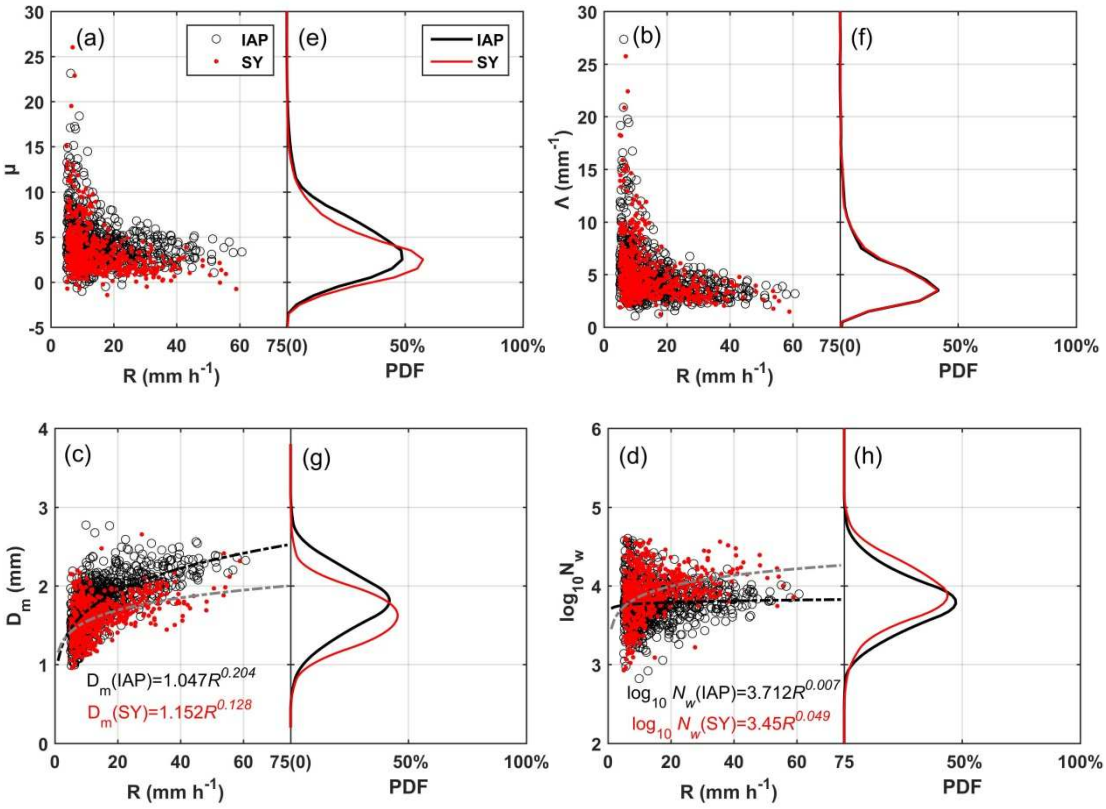

Fig.9. The scatterplots of (a) μ, (b) Λ (mm^{-1}), (c) D_m(mm), and (d) $\log_{10}N_w$ (N_w: m^{-3} mm^{-1}) versus R (mm h^{-1}) for each 1-min DSD observed by PARSIVEL at IAP (black circle) and 2DVD at SY (red dot). The probability density functions (PDFs) (e-h) of the DSD parameters observed from SY-2DVD (solid red line) and IAP-Parsievl^2 (solid black line) are also given in each panel. The black dashed line (IAP) and gray dashed line (SY) in the left panel of Figs. 9c and9d represent the fitted D_m-R and $\log_{10}N_w$-R relations at the two sites, respectively.

3.2.5. Distributions of D_m and N_w

Previous studies (e.g., Bringi et al., 2003; Thompson et al., 2015; Ulbrich and Atlas, 1998) showed that the behaviors of the DSD parameters N_w and D_m are distinctly different for the maritime and continental convective storms. Fig. 10 shows the scatterplots of D_m versus $\log_{10}N_w$ at the two stations during different stages of the rainstorm. During S1, most of the D_m - $\log_{10}N_w$ pairs observed by 2DVD at SY appear on the left side of the stratiform line according to Bringi et al. (2003) while a few samples appear on the right side (Fig. 10a) due to a strong convective rain cell over the site. Fig. 10b shows the mean values of D_m and $\log_{10}N_w$ at sites IAP (white triangle) and SY (red triangle) during the stratified rain in S2; these values are close to the summer stratiform rain measured in eastern China (Wen et al., 2016), but smaller than those in southern China (Zhang et al., 2019), as marked by cyan symbols in Fig. 10b. However, both $\log_{10}N_w$ and D_m are smaller than those for convective rainfall (S3) observed in southern China where $\log_{10}N_w$ is 4.36 and D_m is 2.21 mm (magenta square symbol in Fig. 10c). Compared with the convective rainfall in eastern China (magenta dot in S3, $\log_{10}N_w$:3.81, D_m: 0.76 mm), D_m is slightly larger, while $\log_{10}N_w$ is smaller. Smaller $\log_{10}N_w$ and larger D_m (or D_0) may be related to the aerosol concentration and cloud condensation nuclei (CCN) (May et al., 2011). With increased aerosol loading, warm-rain processes in convective clouds, such as collision-coalescence and breakup of raindrops can be suppressed, resulting in smaller raindrop concentrations (Chen et al., 2013; Miltenberger et al., 2015).

For convective rain, Bringi et al. (2003) found that the DSDs of convective systems could be divided into two distinct clusters. One group is a "maritime-like" cluster with $\langle D_m \rangle$ = 1.5-1.75 mm and $\langle \log_{10}N_w \rangle$=4-4.5 (the cyan rectangle in Fig. 10). The other group is characterized by $\langle D_m \rangle$ = 2-2.75 mm and $\langle \log_{10}N_w \rangle$ = 3-3.5 and is referred to as the "continental-like" cluster (the orange rectangle in Fig. 10). S3 is a convective precipitation stage, and the D_m-$\log_{10}N_w$ data points mainly appear between

the maritime and continental convective clusters (Fig. 10c). Interestingly, the mean values of D_m and $\log_{10}N_w$ at IAP are closer to the continental convection cluster, indicating lager raindrop diameters with a mean D_m of ~1. 9 mm (white triangle symbol in Fig. 10c) and lower raindrop concentrations with a logarithmic N_w of ~3.7 compared with the SY observations which are more similar to maritime convection. Only a few D_m-$\log_{10}N_w$ data points from the S4 stage (Fig. 10d) appear in the orange rectangle observed for continental convective clusters in Bringi et al. (2003). In addition, the raindrops with D_m < 1 mm noticeably increase from S3 to S4 and D_m-$\log_{10}N_w$ pairs observed at IAP fall in the "maritime-like" cluster during S4, indicating that the microphysical characteristics of this inland rainstorm evolved from "continental-like" convection (i.e., S3) to "maritime-like" convection (S4) due to the abundant moisture transport from the Bohai Sea. The mean values of $\log_{10}N_w$ during S3 and S4 at both sites are 3.7 and 4.1, respectively, which are distributed around the $\log_{10}N_w$ =3.85 line given by Thompson et al. (2015), implying that the microphysical characteristics of the convective stage of this rainstorm also approached those of tropical and oceanic convective rainfalls in equatorial Indian Ocean. During S5, D_m ranges from 0.3 to 2.7 mm and the $\log_{10}N_w$ ranges from 1.8 to 5.3. The wide ranges of D_m-$\log_{10}N_w$ pairs are mainly attributed to the scattered rain cells passing over the two sites. Moreover, shallow precipitation (yellow dots in Figs. 10d, e) also observed during both S4 and S5 with D_m ~0.5-1.0 mm, and $\log_{10}N_w$ ~4-5.5. In summary, the characteristics of the D_m and N_w values during this event imply that extreme rainfall was mainly composed of high concentrations of small and medium-sized drops. This conclusion is further illustrated in Table 3. Small raindrops (D<1 mm) dominate the total concentration (~87.6%) of the total data set, accounting for 21.8% of the total water content and 10.8% of the total rainfall but have the smallest contribution to reflectivity. The contributions of small and medium-sized raindrops (D: 1~2 mm) to the total rainfall and water content are greatest, accounting for 54.5% and 53.2%, respectively, and decrease sharply with increasing drop diameter. The particles that contribute the most to the reflectivity are the medium-sized particles of 2 ~ 3 mm. The contributions of small and medium-sized raindrops (D < 4 mm) to total precipitation, water content and reflectivity are more than 97%, while the contribution of larger raindrops (D > 4 mm) is negligible (< 3%). This result is consistent with the conclusion shown of Figs. 7a and c that raindrops for this heavy rainfall in northern China were mainly concentrated in small sizes.

In summary, the DSD difference between the two sites in the same climate regime is almost negligible during stratiform precipitation (S2), while the microphysical characteristics of convective precipitation (S3 and S4) are very different even in the same cloud-precipitation system. In the two stages of strong convective precipitation, from S3 to S4, the microphysical characteristics of this rainfall transformed from the "continental-like" cluster to the "maritime-like" cluster even though Beijing is located in an inland area. This effect was likely due to the ample supply of moisture transported from the Bohai Sea to this study region by the mesoscale circulation, resulting in a deep warm cloud layer and preventing small drops from evaporating before they reached the surface. The persistent production of small drops involves active coalescence and breakup of raindrops, implying that collisional breakup was one of the main mechanisms that determined the DSD shapes in the convective stages of this rainstorm.

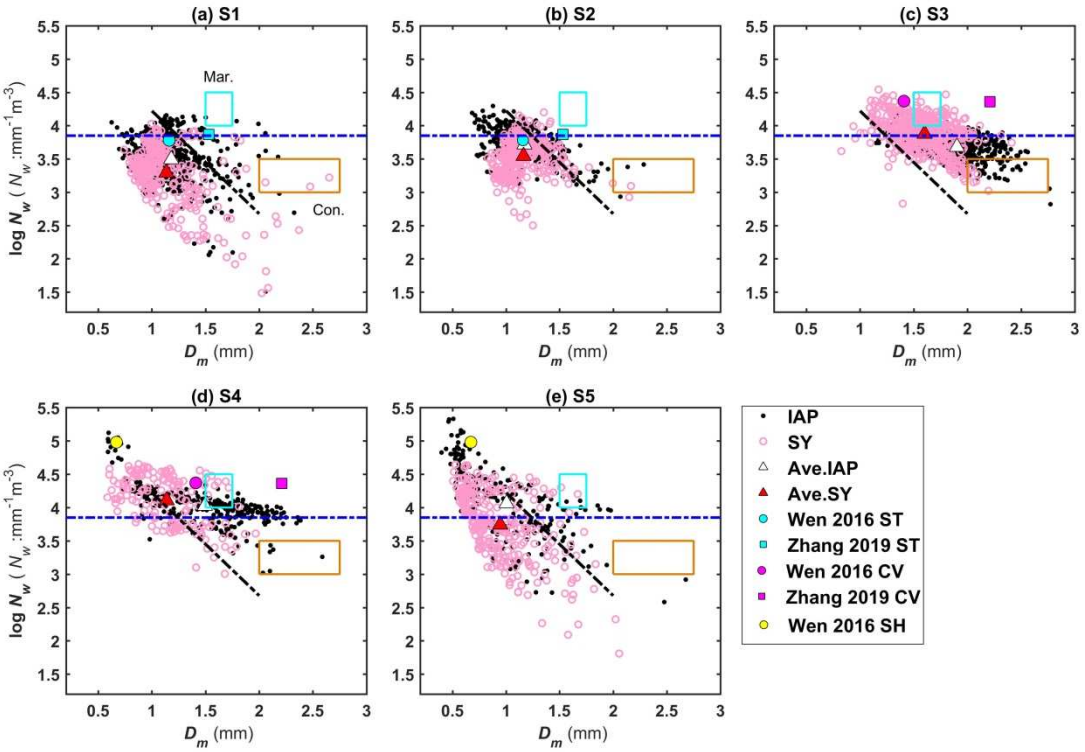

Fig.10. (a-e) Scatterplots of D_m and $\log_{10}N_w$ obtained from the 2DVD (red circles) and Parsivel^2 (black dots) data for the whole storm event. The mean values of N_w and D_m are represented by triangle symbols (red for SY and white for IAP). The two rectangles correspond to the maritime (cyan) and continental convective (orange) clusters reported by Bringi et al. (2003). The black and purple dash-dot lines represent the characteristics of stratiform rain described in Bringi et al. (2003) and the convection/stratifrom separation line from Thompson et al. (2015), respectively. The square symbols and circles represent the average values of various types of rain, from Zhang et al. (2019) and Wen et al., (2016), respectively. CV stands for convective rain, ST is stratiform rain and SH is shallow rainfall.

Table 3 Relative contributions of each size class to the total drop concentration N_t, liquid water content W, rain rate R and reflectivity Z for the whole data set.

***D*(mm)**	<1	1~2	2~3	3~4	>4
No. of drops	1504052	682369	85816	4560	141
***N*$_t$ (%)**	**87.61**	11.33	1.01	0.05	0.0015
***W*(%)**	21.81	**53.17**	21.92	2.89	0.18
***R*(%)**	10.80	**54.51**	**29.89**	4.44	0.30
***Z*(%)**	1.49	**30.59**	**47.59**	16.90	2.29

3.2.6. Temporal variations in DSDs observed by 2DVD

The variations in raindrop size and the shapes of drop size distributions are related to the physical processes in the cloud-precipitation system, such as the collision–coalescence processes in warm, shallow, convection rainfall of oceanic origin (Tokay et al., 2008). Based on the field observations, we can explore the variations in the DSDs of different rain types when the precipitation system moves over the stations in different rainfall stages.

We select the 1-minute DSDs observed by 2DVD where the size bin is uniform, which may allow us to resolve the breakup signatures better than the Parsivel^2 samples with smoother DSD curves due to the larger width of DSD bins (D'Adderio et al., 2015). The 1-min DSDs were averaged over a 10-min scale for this long-lasting rainfall event. This averaging was calculated as a trade-off between the need for a fine temporal scale of the precipitation structure and the clarity of the DSD representation (Porcù et al., 2013; Porcù et al., 2014). The 10-min average rain rate is plotted in Figs. 11a-[A-B] and Figs.

11b-[A-F], with corresponding 10-min DSDs shown in Figs. 11a-[A'-B'] and Figs. 11b-[A'-F']. Note that Fig. 11a reports S1 split in two smaller parts (Fig. 11a-[A] and Fig. 11a-[B], respectively). Fig. 11b reports S2 (Fig. 11b-[A]), S3 (which is split in two parts, Fig. 11b-[B] and Fig. 11b-[C], respectively) and S4 (Fig. 11b-[D]).

In the top panel of Fig. 11a, two separate peaks in the 10-min rain rate are observed at approximately 6.2 mm h^{-1} between 08:00 and 10:00 LST 19 July (Fig. 11a-[A]) and 7.8 mm h^{-1} from 12:00 to 16:00 LST 19 July (Fig. 11a-[B]). The two rain rate peaks are characterized by significant increases in the number of drops for almost all diameters and marked increases in the number of drops larger than 1.5 mm, which contribute to the increase in the rain rate by a factor of 2 or even higher. At the same time, the DSD (light green curve in Fig. 11a-[A'] corresponding to the rain rate peak show a secondary peak at approximately 1.5 mm, indicating that the equilibrium DSD (EDSD) (D'Adderio et al., 2015; Porcù et al., 2014) may have been reached during this 10-min duration. The orange and red curves in Fig. 11a-[A'] also present a 2-peak or even multipeak shape during the light rain, which may be related to the low numbers of raindrops that lead to sharp discontinuities near the edge of the rain band. Many DSDs present a single peak at approximately 0.5 mm during S2 (Fig. 11b-[A']). As shown in Fig. 11b-[A], the 10-min rain rate is below 6 mm h^{-1}, and the 2-min rain rate is less than 10 mm h^{-1}. In addition, the highest slope (HS) values (D'Adderio et al., 2015, 2018) based on 2-min DSD are all negative (-3.3 ~ -1.2), indicating many steep DSDs with almost all raindrops smaller than 3.0 mm.

From 08:10 to 16:30 LST 20 July, the 10-min rain rate ranges from 2.7 to 34.4 mm h^{-1} (Figs. 11b-[B-C]), and the DSDs in Fig. 11b-[B'] have a well-defined peak at 0.3 mm and then a sharp decrease in the number of drops from the peak to approximately 0.9 mm where an obvious inflection point is also present, followed by a relatively slower decrease between 1.0 mm and 2.0 mm, indicating the breakup of raindrops (D'Adderio et al., 2015). However, EDSD was not reached. Several bimodal structures of 10-min DSD occurred between 16:00 LST and 17:00 LST 20 July, as shown by the red curves in Fig. 11b-[C'], which have a first peak at 0.3 mm and a second peak at approximately 1.1mm, indicating that EDSD may have been reached (D'Adderio et al., 2015, 2018; Low and List, 1982; McFarquhar, 2004; McTaggartcowan and List, 1975). DSDs from 02:00 to 17:00 LST 20 July (Fig. 11b-[B'-C']) have more similar shapes. These results reflect the steady and statistically homogeneous or equilibrium rainfall during the mature, most intense convective rainfall episode (Steiner et al., 2004). During the episode between 17:00 LST and 20:12 LST 20 July, the SY site was marginally touched by the rainstorm with the highest 10-min rain rate of 34 mm h^{-1}(Fig. 11b-[D]), characterized by a bimodal DSD (gold curve in Fig. 11b-[D']), which also implies that an EDSD was reached.

The EDSD is usually detected in cases of a relatively rapid precipitation rate increase (D'Adderio et al., 2018). Because of the short lifetime of an EDSD, a close inspection of DSDs averaged over two minutes during the increasing rain rate period between 13:20 and 14:00 LST 20 July is analyzed, as reported in Fig. 12. Two separate high rain rate peaks, 65 mm h^{-1} at 13:30 LST and 56 mm h^{-1} at 13:48 LST, are observed during this episode (Fig. 12a). A DSD shape with a single peak is observed at 13:20 LST, and a DSD with an inflection point at 1.0 mm starts to emerge 3-4 minutes later (blue curve in Fig. 12b). At 13:28 LST, the maximum diameter reaches 3.5 mm, and drops from 0.9-1 mm are weakly depleted, indicating the breakup signal at this moment. Soon after, the rain rate reaches a maximum of 65 mm h^{-1} (13:30 LST) and DSD reaches the equilibrium (aquamarine cross line in Fig. 12b). In the next 2 minutes, the number concentration of small raindrops (D<1.0 mm) is almost unchanged, but the number of mid-sized drops (1<D<4 mm) decreases rapidly, reducing the rain rate to 20 mm h^{-1}. That is, the rain rate decreases by nearly 70% compared to the last moment (13:30 LST). This result indicates that the rainfall rate is highly sensitive to the number concentration of the medium-sized raindrops and exhibits a number concentration-controlled DSD variability during this strong convection episode (Steiner et al., 2004). The ginger curve in Fig. 12b shows a sharp decrease in drops with diameters less than 3 mm, and a weak change in concavity is present between 0.5 and 2.3 mm, indicating that some other processes (Radhakrishna and Rao, 2009) occurred between 13:32 and 13:34 LST, preventing equilibrium between breakup and coalescence and the maintenance of EDSD. However, the collisional breakup soon returns to its dominant role until 13:42 LST (brown and purple curve in Fig. 12b), keeping the rain rate at approximately 25 mm h^{-1} from 13:36 to 13:42 LST. At 13:44 LST, the rain rate decreases to 10 mm h^{-1}, and the DSD shows a single peak shape. In the next interval of continuous

heavy precipitation lasting near 16 minutes, almost all the drop spectra have an obvious inflection point at 1.0 mm and there is a well-defined peak at 0.3 mm, but we do not find a second significant peak. These results indicate that even if the rainfall intensity increases significantly in a short time, there is still no EDSD observed in this process, and other microphysical processes may be dominant to modify the DSDs, rather than collisional breakup of drops.

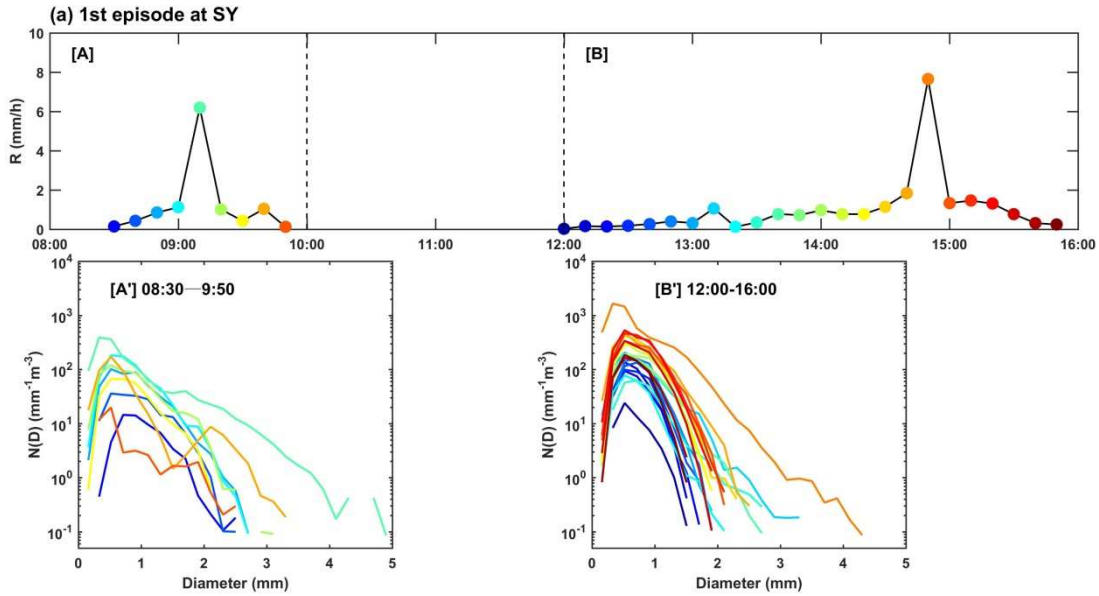

(a) The time series of the 10-min rain rate and DSDs during the 1st episode of the "7.20" rainstorm.

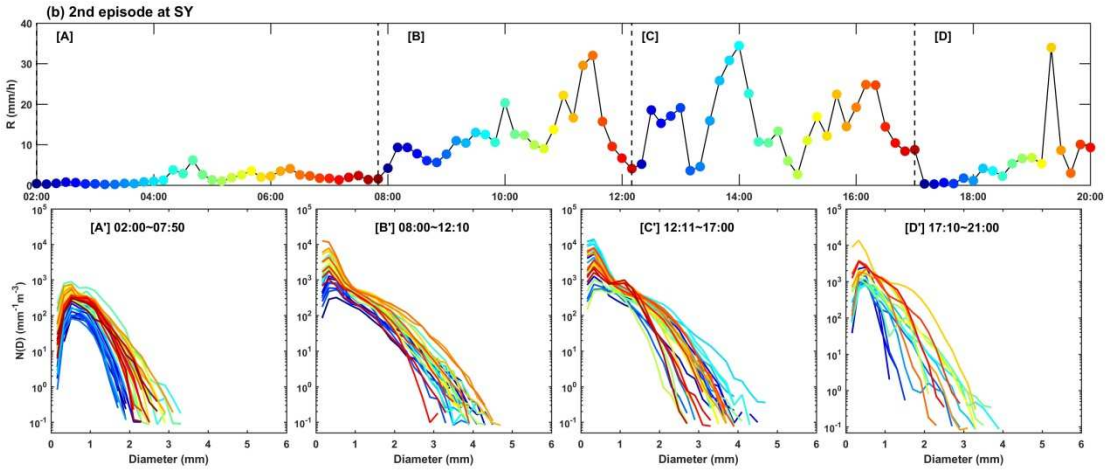

(b) As in **(a)** but for the 2nd episode.

Fig.11. The time series of the 10-min rain rate and DSDs (at SY) during the two episodes of the "7.20" rainstorm: **(a)** the 1st episode from 08:00 to 16:00 LST 19 July; **(b)** the 2nd episode from 02:00 to 20:00 LST 20 July. In (a), the DSD plots of [A'] and [B'] correspond to the rain rate time series of [A] and [B], respectively. Similarly, in (b), [A']-[D'] correspond to [A]-[D]. The color in the time series of rain rate matches the color used in the DSD plots, which essentially stands for different time frames.

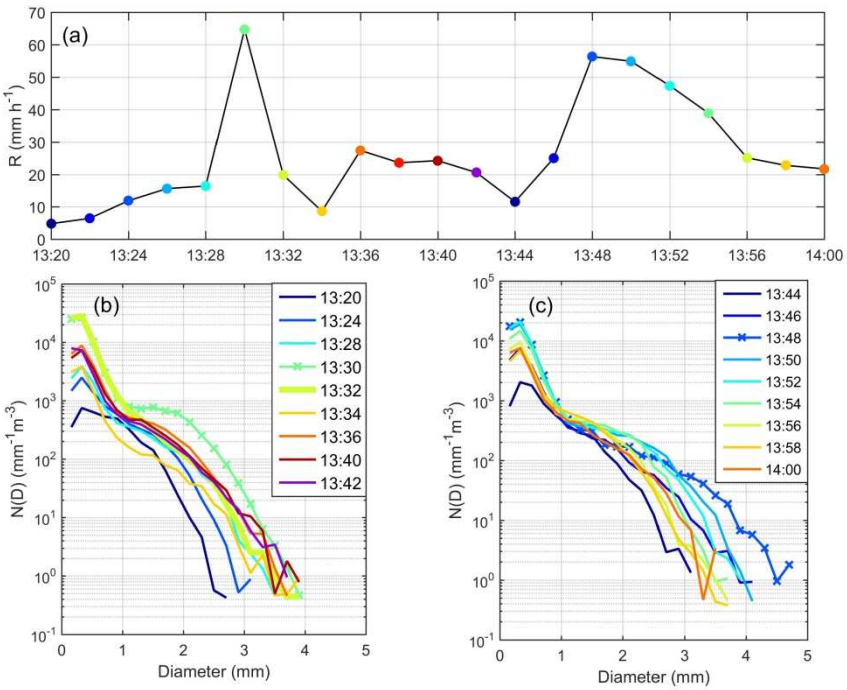

Fig. 12. The time series of the 2-min rain rate **(a)** and DSDs **(b-c)** (at SY) between 13:20 and 14:00 LST 20 July. The cross lines in Fig. 12 **b** and **c** are correspond to the rain rate peaks.

3.2.7. Mean drop spectra and gamma DSD model

Figs. 11 and 12 indicate that the evolutions and shapes of the DSDs are closely related to the changes in rainfall rate. Hence, the behaviors of composite DSD for six different rain rate intervals are investigated based on the 1-min DSD data. We classify the rainfall rates R (mm h^{-1}) into 6 classes as follows (Porcù et al., 2014): 0. $1 \le R < 1$ (class 1, 296 minutes), $1 \le R < 2$ (class 2, 140 minutes), $2 \le R < 5$ (class 3, 242 minutes), $5 \le R < 10$ (class 4, 238 minutes), $10 \le R < 20$ (class 5, 186 minutes), and $R \ge 20$ (class 6, 117 minutes). Fig. 13 shows the changes in $N(D)$ (m^{-3} mm^{-1}) at different rain rates, and the gamma distribution fitted on each composite spectrum using the 2-3-4 moment method (M234) is also plotted. Here, we chose the M234 method after comparing M234 with other moment methods (i.e., 0-1-2 and 2-4-6 moment methods), and the M234 showed the best fitting effect with respect to the other moments. The corresponding gamma distribution parameters N_0 ($mm^{-1-\mu}$ m^{-3}), μ and Λ (mm^{-1}) are detailed in Table 4a. In addition, the gamma model-derived DSD values are compared with actual measurements to validate the empirical model. To quantify the performance of the gamma model in each rain rate class, the normalized absolute error (NE), root mean square error (RMSE), and correlation coefficient (CC) are calculated as follows:

$$NE = \frac{\frac{1}{N}\sum_{d=1}^{N}(ND_{gamma,d} - ND_{obs,d})}{\overline{ND_{obs}}} \tag{14}$$

$$RMSE = [\frac{1}{N}\sum_{d=1}^{N}(ND_{gamma,d} - ND_{obs,d})^2]^{1/2} \tag{15}$$

$$CC = \frac{\sum_{d=1}^{N}(ND_{gamma,d} - \overline{ND_{gamma}})(ND_{obs,d} - \overline{ND_{obs}})}{[\sum_{d=1}^{N}(ND_{gamma,d} - \overline{ND_{gamma}})^2]^{1/2}[\sum_{d=1}^{N}(ND_{obs,d} - \overline{ND_{obs}})^2]^{1/2}} \tag{16}$$

where N is the total number of bins; $ND_{gamma,d}$ and $ND_{obs,d}$ are the gamma modeled and actually measured DSD for size bin d, respectively. The symbol "‾" represents the sample average. The values of NE, RMSE and CC are listed in Table 4b.

As shown in Fig. 13, the number concentration of raindrops is very sensitive to changes in rain intensity. When the rain rate is less than 5 mm h^{-1} (classes 1, 2 and 3), the DSDs show a concave-down

shape and have a single peak at approximately 0.5 mm, indicating that they are described by a DSD having μ>0. Notably, a clearly defined transition in the DSD shape appears between classes 3 and 4, and a distinct inflection point of approximately 0.7 mm appears. When the rainfall intensity exceeds class 4, where convective episodes are likely to occur, raindrops between 0.5 mm and 1.5 mm are depleted, while there is an increase of small drops (less than 0.5 mm) and small- to medium-sized drops around 1.5-3 mm so that an inflection point shows up in the DSD between 0.5 mm and 1.5 mm. The peak at small diameters is more distinct than the one at larger size. The number concentrations of drops before and after the inflection point increase with the rain rate, making a bimodal DSD gradually emerge. This change implies that the equilibrium breakup of raindrops begins to occur at a moderate rainfall intensity (class 4), resulting in a significant increase in small raindrops. In addition, it is concluded that the increase in rain rate is mainly due to the increase in drop numbers for almost all diameters. Fig. 13 shows clearly that the gamma distribution fits better the DSD in the middle range of the spectrum while deviating from smaller and larger diameters, especially for higher rain rate (like classes 5 and 6), where the bimodal DSD occurs.

As shown in Table 4a, the three parameters N_0, μ and Λ of gamma DSD decrease with the increasing rain rate. The correlation of the DSD derived from the gamma model with the actual DSD data is greater than 0.93 for rain rates less than 10 mm h^{-1} (Table 4b). As expected, the correlation coefficient (CC) decreases as the rain rate increases and reaches a minimum value of approximately 0.82 when the rain rate exceeds 20 mm h^{-1}. In contrast, the RMSE and NE for rain rates larger than 1 mm h^{-1} increase with the rain rate. The lowest CC and highest RMSE and NE appear at rain rates exceeding 20 mm h^{-1}, indicating that the gamma model represents the DSD measurements of heavy rainfall not so well, although it is more suitable for modeling the DSDs in stratiform rainfall where the rain rate is less than approximately 10 mm h^{-1}. This outcome suggests that gamma distribution does not represent well the breakup-induced bimodal DSD in relatively high rain rate (R>10 mm h^{-1}). In an attempt to alleviate this problem, our future work is to seek which mathematical model can represent bimodal DSD more appropriately to provide a reference for the DSD retrieval from dual-polarization radar and/or satellite observations.

Table 4a Gamma distribution parameters N_0 ($mm^{-1-\mu}\,m^{-3}$), μ and Λ (mm^{-1}) derived from the composite raindrop spectra in six rain rate classes using the 2-3-4 moment method

rain rate (mm h^{-1})	**N_0 ($mm^{-1-\mu-3}$)**	**μ**	**Λ mm^{-1})**
0. 1 ≤ R < 1 (class 1)	139990	3.40	7.68
1 ≤ R < 2 (class 2)	127390	3.28	6.50
2 ≤ R < 5 (class 3)	39976	2.33	4.90
5 ≤ R < 10 (class 4)	18220	1.47	3.64
10 ≤ R < 20 (class 5)	17732	1.05	3.18
20 ≤ R (class 6)	11126	-0.01	2.21

Table 4b The CC, RMSE and NE calculated between the gamma models and actual measurements in the six rain rate classes

rain rate (mm h^{-1})	**CC**	**RMSE (m^{-3} mm^{-1})**	**NE**
0. 1 ≤ R < 1 (class 1)	0.93	15.00	0.22
1 ≤ R < 2 (class 2)	0.99	15.33	0.13
2 ≤ R < 5 (class 3)	0.99	21.50	0.11
5 ≤ R < 10 (class 4)	0.96	67.47	0.16
10 ≤ R < 20 (class 5)	0.87	214.46	0.28
20 ≤ R (class 6)	0.82	733.60	0.32

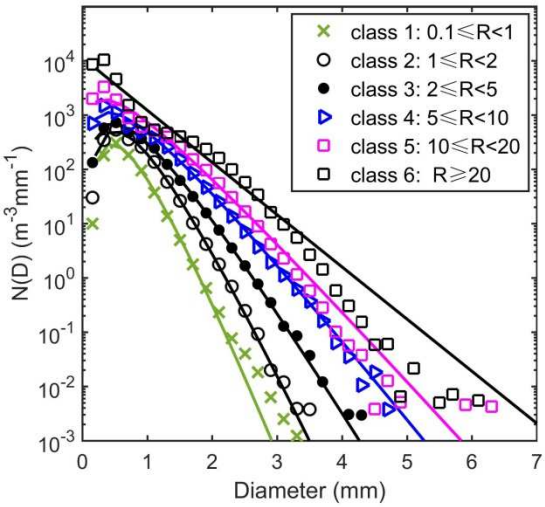

Fig.13. Mean DSDs observed by 2DVD at station SY during the "7.20" rainstorm. The DSD data are averaged using different rain rate thresholds. The fitting curves are based on the 2-4-6-moment method.

3.3. Vertical structures

As shown in Fig. 14, the contoured frequency-by-altitude diagrams (CFADs) (Yuter and Houze, 1995) for different variables (reflectivity Z (dBZ), drop fall velocity V (m s^{-1}), and liquid water content W (g m^{-3})) during each rain stage are analyzed to resolve the evolution of the vertical structure of microphysical processes during this storm. We use the changes in the frequency distributions of the three parameters (i.e., *Z, V, W*) to study the microphysical processes of different rainfall types including stratiform rain (S2, as shown in the first column in Fig. 14) and the two convection phases (S3 and S4 in the second and third columns in Fig. 14, respectively) of this rainstorm. Note that the 0℃ isotherm (approximately 4.62km above sea level) is averaged from all the *in situ* sounding data, which are collected twice a day during precipitation episodes. Fig. 14 shows the vertical profiles from 0.3 km to 3.1 km, which are generally in the liquid phase toward the surface. For the stratiform episode, as shown in the first column in Fig. 14, the CFADs of Z, $\log_{10}W$ and V present approximately uniform distributions, and the mean profiles of the three parameters also vary little with height, suggesting that raindrop evaporation and coalescence are in near balance during the stratiform rainfall episodes.

In contrast to stratiform rain, the convective CFAD in the second column exhibits relatively different features with the height. Reflectivity, water content and drop fall velocity reach their maximum values and their average values increase with decreasing altitude (see the yellow solid line in Figs. 14b, e, h), implying significant changes in drop number and diameter due to the cloud microphysical processes. In addition, the distributions of $\log_{10}W$ and V (m s^{-1}) below 1 km are slightly narrower than those above 1 km (Figs. 14e, h), whereas the distribution of Z dominated by medium to large drops remains unchanged (Fig. 14b), which may be related to the combination of the coalescence and breakup of raindrops, accretion with cloud droplets, and evaporation of small drops. Moreover, the reflectivity with probability more than 30% is concentrated within 30–38 dBZ below ~2 km (Fig. 14b), but it is distributed between 15 and 25 dBZ in S1 (Fig. 14a). The distribution of reflectivity in convective rainfall is narrower than that in stratiform rainfall, further indicating that coalescence and collisional processes are more active in the convective precipitation episodes.

The mean values of Z, W and V during S4 (the yellow solid line in the 3rd column) are higher (lower) than those in S2 (S3) at the same height, due to an isolate convective rain cells passing over Beijing during S4 (ref. Fig. 5d). In addition, the distributions of drop fall velocity V (Fig. 14f) and (less evident) of logarithmic content W (Fig. 14i) are relatively uniform with height and wider than those during S2 and S3 at the same level, which is probably related to the more variability in the DSD in S4 (Fig. 11b-[D]) with respect to the other periods of the second episode at SY.

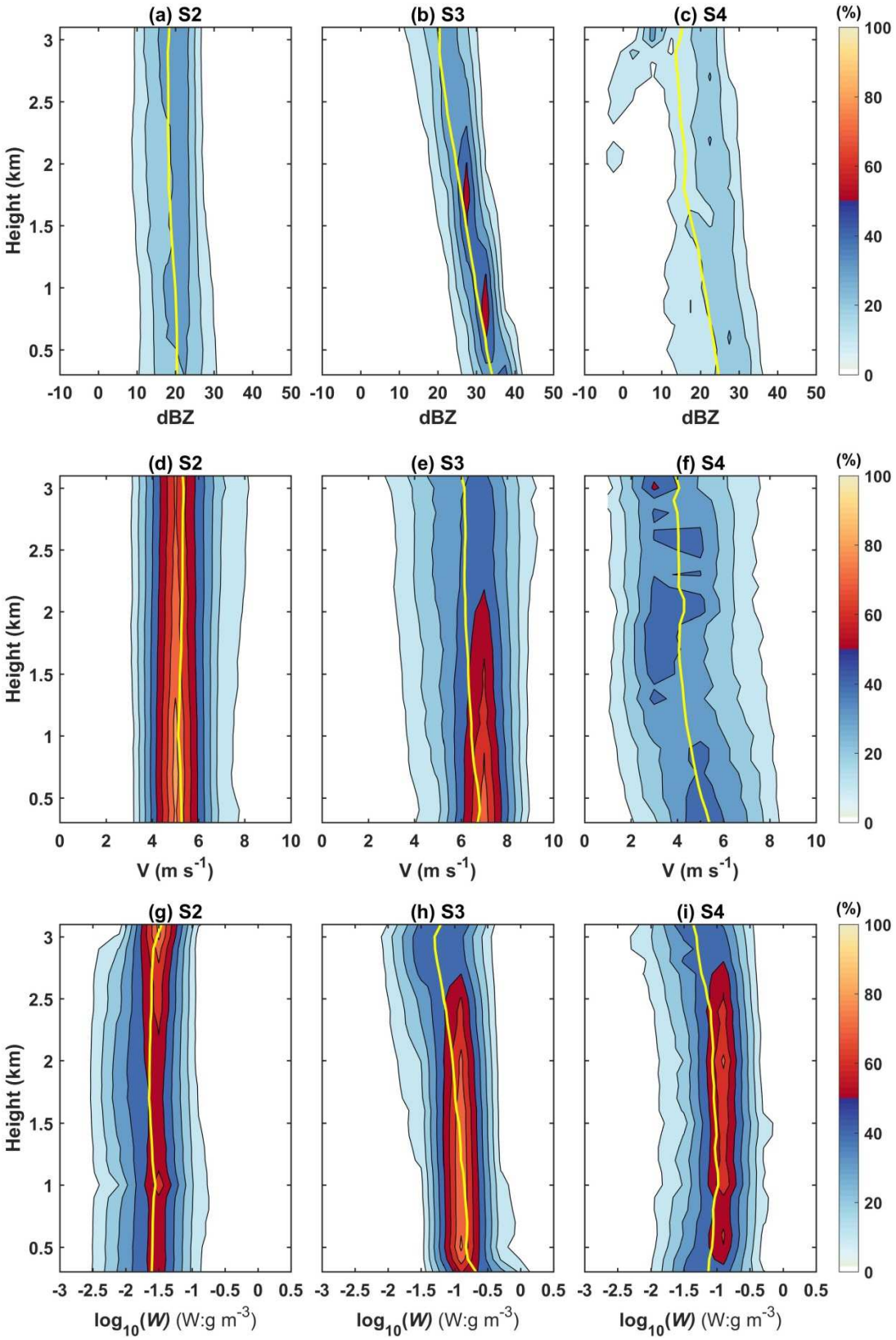

Fig.14. Contoured frequency-by-altitude diagrams (CFADs) of (a-c) radar reflectivity Z, (d-f) drop fall velocity V and (g-i) logarithmic liquid water content $\log_{10}W$ in different rainfall stages (from S2 to S4). The solid yellow lines represent the average values in the diagrams. Contours stand for the frequency of occurrence (contoured every 10%) related to the maximum absolute frequency in the data sample represented in the CFAD with the minimum contour level at 10%.

3.4. Z-R relationships

The rainfall algorithm implemented by the operational Doppler weather radar in China is a simple power law $Z(R)$ relation: $Z=AR^b$, where the coefficient A and exponent b are derived from Eqs. (7) and (9) using a least squares method. Many studies (Kumjian and Ryzhkov, 2012; Ryzhkov et al., 2005; Seliga and Bringi, 1976) have shown that such a relation has substantial uncertainty caused by a variety of drop size distributions. The discussion in Section 3.2.5 shows that the DSDs and rainfall parameters D_m and N_w vary with different stages of rain band. In the following, these impacts on *Z-R* relationship are investigated. As shown in Fig. 15, the power-law *Z–R* relationships for five rain phases of this storm at both stations are derived. For comparison, the standard NEXRAD relation $Z = 300R^{1.4}$ (Fulton et al. 1998), which is used in the operational weather radar systems in China, is also plotted in each panel (the blue dashed line).

The coefficient A and exponent b of the *Z-R* relationships vary in each stage due to different cloud microphysical processes. Compared to other episodes, smaller distinctions between the two stations appear during S1 and S3 (Figs. 15a,c), and *Z-R* relations derived for both sites are close to the standard NEXRAD *Z-R* relationship since the two sites were simultaneously covered by large-scale convective precipitation during S3 (Fig. 15c). More strong convective rainfall cells passed over the IAP site during S4. The D_m observed by Parsivel^2 at IAP in S4 ranges widely from 0.6 to 2.6 mm, and almost all $\log_{10}N_w$ points fluctuate below the value of 4±0.3 except for a few points showing very high or low $\log_{10}N_w$ (Fig. 10d), indicating that the variations in DSD observed at IAP during this convective phase are mainly governed by variations of drop size (Steiner et al., 2004). As a result, the maximum b (1.6) and smallest A of the *Z-R* relationship occur at the IAP site during S4. In general, the differences in exponent b at different locations within this storm are no more than 0.2, but the differences between the coefficients A are much larger. Although these differences may be partly caused by the two measurement instruments, the uncertainty of *Z-R* relationships induced by the variations in raindrop size or number concentration or a combination of these factors is obviously much larger.

Fig. 16 further illustrates the DSD variability of different rainfall types. D_m and $\log_{10}Nw$ explain most of the variability of *Z-R* relationships in this rainstorm. The *Z-R* distribution is color coded by mass-weighted mean diameter D_m and logarithmic number concentration $\log_{10}N_w$ using the SY dataset (similar results are found for the IAP site; not shown), akin to the rain parameter diagram in (Steiner et al., 2004; Thompson et al., 2015; Ulbrich and Atlas, 1978;Ulbrich and Atlas, 1998). Low D_m (<0.75 mm; blue dots) values exist only in the lower *Z-R* space with the smallest A value (81.9) and the highest b value (1.08) (Fig. 16a). However, large D_m (>1.75 mm; red dots) values appear in the convective $Z(R)$ distribution (S3 in Fig. 15c). The values of A in *Z-R* relationships increase with increasing D_m and decrease with enhanced $\log_{10}N_w$. In contrast, the variability in exponent b, ranging from 1.03 to 1.08 mm for different D_m and 1.42 to 1.5 in different $\log_{10}Nw$, is slightly less sensitive to D_m and/or $\log_{10}N_w$. In other words, high uncertainty in the *Z-R* relationship is contributed by the combination of variations in drop size and number concentrations, leading to significant uncertainty in the selection of the *Z-R* relationship for QPE. The accuracy of precipitation estimation could be substantially improved if we could predict the rainfall type and subsequently apply an appropriate *Z-R* relationship.

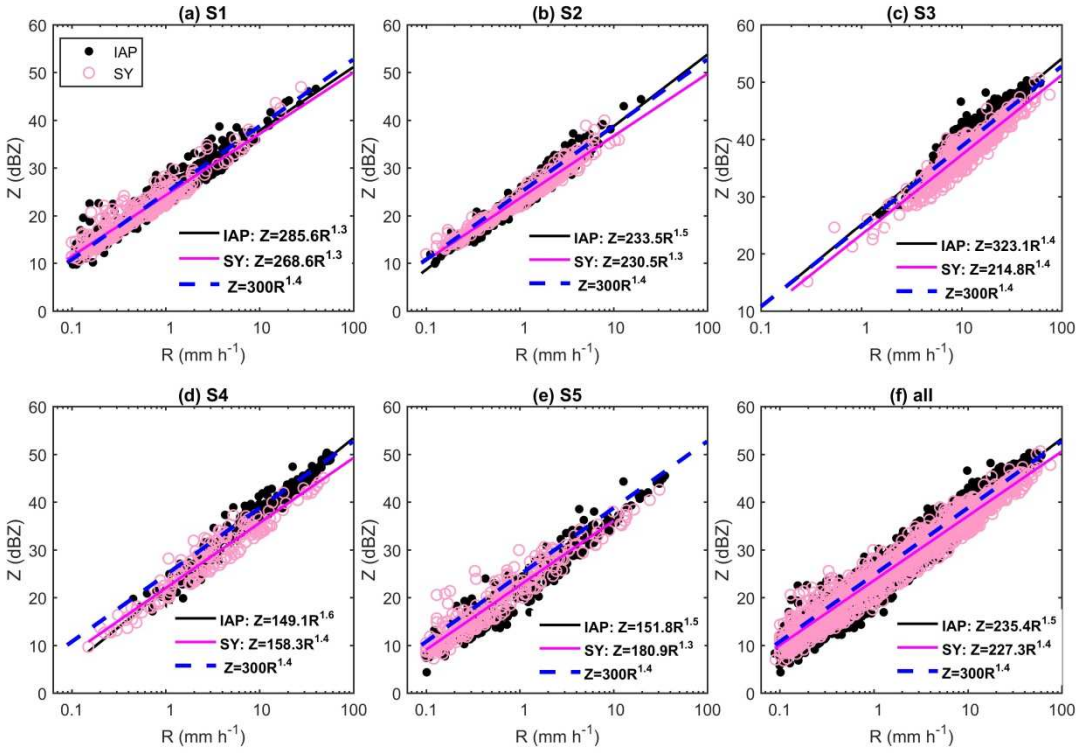

Fig.15. The *Z-R* scatter diagrams based on the 1-min DSD data collected at stations IAP (dark dots) and SY (pink circles) during the five stages (a-e) and (f) the whole event. The fitting relationships between the corresponding *R* and *Z* are shown with black (IAP) and magenta (SY) lines. The blue dashed lines represent the standard NEXRAD *Z-R* relationship ($Z=300R^{1.4}$).

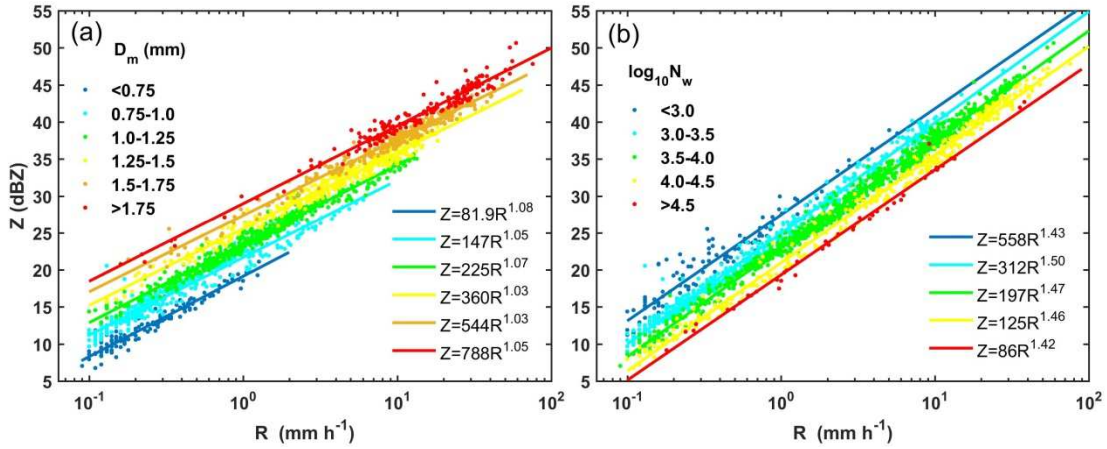

Fig.16. *Z(R)* relations derived from 1-min DSDs recorded at SY overlaid with the color-coded distributions of D_m and $\log_{10}N_w$.

4. Summary and conclusions

In this paper, the microphysical characteristics of the "7.20" extreme rainstorm event that occurred in northern China from 19 to 21 July 2016 are extensively analyzed based on Parsivel^2, 2DVD, and MRR observations. Based on the 1-minute raindrop size data observed by two disdrometers and vertical rainfall profiles obtained by MRR^2, radar reflectivity, precipitation intensity, liquid water content, median volume diameter D_0 and mass-weighted mean diameter D_m of raindrops, as well as the evolution characteristics of DSD, are derived and investigated. This study mainly focuses on the variations in disdrometer-measured drop size distributions as functions of location and time. Moreover, the rainfall microphysical characteristics of this rainstorm are briefly compared with those of other rainfalls in the Meiyu Season in eastern China and the monsoon season in southern China. The analysis

in this paper provides an insight into the microphysical nature of typical heavy rainfall during the summer flood season in northern China, and presents relevant information that may be useful for remote sensing-based rainfall retrievals as well as the parameter optimization of microphysical schemes. The main conclusions are summarized as follows:

(1) The high-level divergence and increased low-level (from ground to 500 hPa) convergence yielded enhanced updrafts and promoted the occurrence, development and maintenance of this mesoscale circulation over northern China. Based on the S-band Doppler weather radar echo structure and ground-based disdrometer observations, this mesoscale circulation was divided into two uninterrupted rain episodes (subdivided into 5 rainfall stages, i.e., S1-S5) to investigate the variability of rainfall characteristics. The frontier of the mesoscale circulation approached the observational domain at approximately 06:00 LST 19 July and continued to move northeastward. During the early rainfall episode (S1), a widespread, long lasting stratiform system with strong embedded convection fell over Beijing, resulting in maximum rain rates of 40.0 mm h^{-1} at IAP and 27.7 mm h^{-1} at SY. The maximum raindrop size was less than 4 mm and the number concentrations of all diameters were less than $10^{3.5}$ m^{-3} mm^{-1} at both the IAP and SY sites.

(2) During the 2nd rainfall episode, from 01:42 LST 20 July to 06:00 LST 21 July, the circulation generated widespread, deep strong convective clouds associated with intense rainfall at the IAP site (R_{max} = 60.7 mm h^{-1}) and the SY site (R_{max} = 75.7 mm h^{-1}), leading to total rainfall of 221.3 mm at IAP and 162 mm at SY. The 2nd rainfall episode was subdivided into four rain stages (S2-S5). S2 was a uniform stratiform precipitation episode lasting approximately 8 hours and the rain rates at the two stations did not exceed 2 mm h^{-1}. During S3, from 08:00 to 16:30 LST 20 July, both sites were covered by a widespread and strong mature convective rain band; large concentrations of small raindrops (D<2 mm) and maximum drop diameters close to 5 mm were observed at both sites. During S4, the circulation moved farther northeast, and a second intense convection rainfall was observed at IAP (R_{max} =57.9 mm h^{-1}) and SY (R_{max} =48.2 mm h^{-1}). After 21:00 LST 20 July, the circulation receded, and SY observed the edge of the rain band before IAP did. During S5, the raindrops were as small as 3 mm with few larger drops (~4 mm) at IAP, and some DSD clusters containing only high concentrations of small drops (i.e., shallow rainfall as documented in Wen et al. (2016) were also observed at both sites.

(3) During the 1st episode, the DSDs showed bimodal shapes at the 10-min rain rate peaks, indicating that the equilibrium DSD may have been reached. The variability of drop spectra was primarily facilitated by a mixture of variations in drop size and number density. In the 2nd episode, more bimodal DSDs were observed; collisional breakup occurred during convective rainfall, and the controlling mechanism for the variability of DSDs seemed to be dominated by the drop size. In the stratiform rain (R<10 mm h^{-1}), the DSD shape was mainly convex with a single peak at 0.5 mm, and the distributions of parameters μ, Λ, D_m and N_w were wider with lower rainfall intensity. However, the range of variation decreased with increasing rain rate and became more uniform at higher rain rates (R > 10 mm h^{-1}), except for D_m, suggesting that the rain rate was mainly due to the increase in raindrop diameter. In addition, the performance of the gamma model in six rain rate classes was quantified, and the correlations between the DSDs derived from the gamma model and the actual DSD data were greater than 0.93 for rain rates less than 10 mm h^{-1}. Nevertheless, the gamma model did not represent the DSD measurements of heavy rainfall very well; the correlation was 0.82, and the highest NE (67%) appeared at rain rates exceeding 20 mm h^{-1}.

(4) The *Z-R* relations derived from two disdrometers during S1 were similar. The coefficient A of the *Z-R* relationships during S2 was similar at the two sites, while the exponent *b* was 1.5 for IAP and 1.3 for SY, reflecting a larger D_0 variability at IAP due to a strong convective rain cell aloft passing by. During S3, both sites were covered by a widespread and strong mature convective rain band; as a result, the number concentration and the variability of D_0 were quite similar at the two sites, leading to two corresponding *Z-R* relationships. In S4 and S5, the coefficients of *Z-R* relationships decreased significantly compared to the previous rainfall episodes at both sites due to the increasing large concentrations of small raindrops. The standard NEXRAD *Z-R* relationship underestimated the rainfall at SY but produced comparative estimates at IAP when the rain rate exceeded 10 mm h^{-1}, although underestimation was observed when the rain rate was less than 10 mm h^{-1}. For statistically homogenous or equilibrium rainfall during this mature stage of the rainstorm, the mean drop number density

remained constant, while intensity variations were accommodated through fluctuations in raindrop size.

Although interesting discoveries have been made from the microphysical analysis of the "7.20" great rainstorm event, future work based on long-term *in situ* observations is still required to fully understand the precipitation mechanisms in northern China.

Acknowledgments

This work was partially supported by the National Key Research and Development Plan of China (Grant No. 2016YFE0201900-02) and the National Natural Science Foundation of China (Grant No. 41575037). The participation of H. Chen was also supported by California Department of Water Resources and the Physical Sciences Division of NOAA Earth System Research Laboratory. We would like to thank Dr. Guang Wen of LACS for his great help in the operation of the 2DVD and data processing. We also would like thank Mr. Long Wen and Mr. Zhengwei Yang at Nanjing University for their help in the calibration and maintenance of the 2DVD.

References

Atlas, D., Srivastava, R.C., Sekhon, R.S.,1973. Doppler radar characteristics of precipitation at vertical incidence. Rev. Geophys. 11, 1-35.

Beate, G.L., Michael, P., 2012. Inter-model variability and biases of the global water cycle in CMIP3 coupled climate models. Environ. Res. Lett. 7 (1), 014006.

Blyth, A.M., Lowenstein, J.H., Huang, Y., Cui, Z., Davies, S., Carslaw, K.S.,2013. The production of warm rain in shallow maritime cumulus clouds. Q. J. R. Meteorol. Soc. 139, 20-31.

Boucher, O., D. Randall, P. Artaxo, C. Bretherton, G. Feingold, P. Forster, V.-M. Kerminen, Y. Kondo, H. Liao, U. Lohmann, P. Rasch, S.K. Satheesh, S. Sherwood, B. Stevens, and X.Y. Zhang., 2013. Clouds and aerosols. In Climate Change 2013: The Physical Science Basis. Contribution of Working Group I to the Fifth Assessment Report of the Intergovernmental Panel on Climate Change. T.F. Stocker, D. Qin, G.-K. Plattner, M. Tignor, S.K. Allen, J. Doschung, A. Nauels, Y. Xia, V. Bex, and P.M. Midgley, Eds. Cambridge University Press, 571-657. doi:10.1017/CBO9781107415324.016.

Brandes, E.A., Zhang, G.F., Vivekanandan, J.,2002. Experiments in rainfall estimation with a polarimetric radar in a subtropical environment. J. Appl. Meteorol. 41, 674-685.

Bringi, V.N., Chandrasekar, V., Hubbert, J., Gorgucci, E., Randeu, W.L., Schoenhuber, M.,2003. Raindrop size distribution in different climatic regimes from disdrometer and dual-polarized radar analysis. J. Atmos. Sci. 60, 354-365.

Cao, Q., Zhang, G., Brandes, E., Schuur, T., Ryzhkov, A., Ikeda, K.,2008. Analysis of video disdrometer and polarimetric radar data to characterize rain microphysics in oklahoma. J. Appl. Meteorol. Climatol. 47, 2238-2255.

Carey, L. D., R. Cifelli, W. A. Petersen, S. A. Rutledge, and M. A. F. S. Dias, 2001: Characteristics of Amazonian rain measured during TRMM-LBA. Preprints, *30th Conf. on Radar Meteorology*, Munich, Germany. Amer. Meteor. Soc., 12A.9. http://ams.confex.com/ams/30radar/techprogram/paper_21229.htm.

Chang, W.Y., Wang, T.C.C., Lin, P.L.,2009. Characteristics of the raindrop size distribution and drop shape relation in typhoon systems in the western pacific from the 2d video disdrometer and ncu C-band polarimetric radar. J. Atmos. Ocean. Technol. 26, 1973-1993.

Chen, B.J., Yang, J., Pu, J.P.,2013. Statistical characteristics of raindrop size distribution in the meiyu season observed in eastern China. J. Meteorol. Soc. Jpn. 91, 215-227.

Chen, H., Chandrasekar, V., Bechini, R.,2017. An improved dual-polarization radar rainfall algorithm (DROPS 2.0): Application in NASA IFloodS field campaign. J. Hydrometeorol. 18, 917-937.

D'Adderio, L.P., Porcu, F., Tokay, A.,2015. Identification and analysis of collisional breakup in natural rain. J. Atmos. Sci. 72, 3404-3416.

D'Adderio, L.P., Porcu, F., Tokay, A.,2018. Evolution of drop size distribution in natural rain. Atmos. Res. 200, 70-76.

Friedrich, K., Higgins, S., Masters, F.J., Lopez, C.R.J.J.o.A., Technology, O.,2013a. Articulating and stationary parsivel disdrometer measurements in conditions with strong winds and heavy rainfall. J. Atmos. Ocean. Technol. 30, 2063-2080.

Friedrich, K., Kalina, E.A., Aikins, J., Steiner, M., Gochis, D., Kucera, P.A., Ikeda, K., Sun, J.Z.,2016. Raindrop size distribution and rain characteristics during the 2013 great colorado flood. J. Hydrometeorol. 17, 53-72.

Friedrich, K., Kalina, E.A., Masters, F.J., Lopez, C.R.,2013b. Drop-size distributions in thunderstorms measured by optical disdrometers during vortex2. Mon. Weather Rev. 141, 1182-1203.

Fulton, R.A., Breidenbach, J.P., Seo, D.J., Miller, D.A., O'Bannon, T.,1998. The WSR-88D rainfall algorithm. Wea. Forecasting. 13, 377-395.

Gou, Y., Ma, Y., Chen, H., Wen, Y., 2018. Radar-derived quantitative precipitation estimation in complex terrain over the eastern Tibetan plateau. Atmos. Res. 203, 286-297.

Guo, C., Xiao, H., Yang, H., Tang, Q.,2015. Observation and modeling analyses of the macro- and microphysical characteristics of a heavy rain storm in beijing. Atmos. Res. 156, 125-141.

Hamada, A., Takayabu, Y.N., Liu, C., Zipser, E.J.,2015. Weak linkage between the heaviest rainfall and tallest storms. Nature Communications 6.

Hu, Z.L., Srivastava, R.C.,1995. Evolution of raindrop size distribution by coalescence, breakup, and evaporation - theory and observations. J. Atmos. Sci. 52, 1761-1783.

Illingworth, A.J., Stevens, C.,1987. An optical disdrometer for the measurement of raindrop size spectra in windy conditions. J. Atmos. Ocean. Technol. 4, 411-421.

Jaffrain, J., Berne, A.,2011. Experimental quantification of the sampling uncertainty associated with measurements from parsivel disdrometers. J. Hydrometeorol. 12, 352-370.

Jakob, C., 2010. Accelerating progress in global atmospheric model development through improved parameterizations challenges, opportunities, and strategies. Bull. Am. Meteorol. Soc. 91, 869-875.

Ji, L., Chen, H.N., Li, L., Chen, B.J., Xiao, X., Chen, M., Zhang, G.F.,2019. Raindrop size distributions and rain characteristics observed by a parsivel disdrometer in beijing, northern China. Remote Sens. 11, 21.

Krajewski, W.F., Kruger, A., Caracciolo, C., Gole, P., Barthes, L., Creutin, J.D., Delahaye, J.Y., Nikolopoulos, E.I., Ogden, F., Vinson, J.P.,2006. Devex-disdrometer evaluation experiment: Basic results and implications for hydrologic studies. Adv. Water Resour. 29, 311-325.

Kruger, A., Krajewski, W.F.,2002. Two-dimensional video disdrometer: A description. J. Atmos. Ocean. Technol. 19, 602-617.

Kumjian, M.R., Ryzhkov, A.V., 2012. The impact of size sorting on the polarimetric radar variables. J. Atmos. Sci. 69, 2042-2060.

Löffler-Mang, M., Joss, J.,2000. An optical disdrometer for measuring size and velocity of hydrometeors. J. Atmos. Ocean. Technol. 17, 130-139.

Löffler-Mang, M., Kunz, M., Schmid, W.,1999. On the performance of a low-cost k-band doppler radar for quantitative rain measurements. J. Atmos. Ocean. Technol. 16, 379-387.

Lopez, P., 2007. Cloud and precipitation parameterizations in modeling and variational data assimilation: A review. J. Atmos. Sci. 64, 3766-3784.

Low, T.B., List, R.,1982. Collision, coalescence and breakup of raindrops .1. Experimentally established

coalescence efficiencies and fragment size distributions in breakup. J. Atmos. Sci. 39, 1591-1606.

Ma, Y., Ni, G., Chandrasekar, V., Tian, F., Chen, H., 2019. Statistical characteristics of raindrop size distribution during rainy seasons in beijing urban area and implications for radar rainfall estimation. Hydrol. Earth Syst. Sci. Discuss.23, 4153-4170.

Marshall, J.S., Palmer, W.M.,1948. The distribution of raindrops with size. J. Meteorol. 5, 165-166.

Mason, B.J., 1954. Physics of clouds and precipitation. Nature. 174, 957-959.

May, P.T., Bringi, V.N., Thurai, M., 2011. Do we observe aerosol impacts on dsds in strongly forced tropical thunderstorms? J. Atmos. Sci. 68, 1902-1910.

McFarquhar, G.M.,2004. A new representation of collision-induced breakup of raindrops and its implications for the shapes of raindrop size distributions. J. Atmos. Sci. 61, 777-794.

McTaggartcowan, J.D., List, R.,1975. Collision and breakup of water drops at terminal velocity. J. Atmos. Sci. 32, 1401-1411.

Miltenberger, A.K., Seifert, A., Joos, H., Wernli, H., 2015. A scaling relation for warm-phase orographic precipitation: A lagrangian analysis for 2d mountains. Q. J. R. Meteorol. Soc. 141, 2185-2198.

Min, A., Liao, Y., Deng, W., 2016. The analysis of the distribution and trend for heavy rainfall based on the precipitation data from 2008 to 2013 in China. Torrential Rain and Disasters. 35, 576-584 (in Chinese).

Munchak, S.J., Kummerow, C.D., Elsaesser, G., 2012. Relationships between the raindrop size distribution and properties of the environment and clouds inferred from trmm. J. Clim. 25, 2963-2978.

Nešpor, V., Krajewski, W.F., Kruger, A.,2000. Wind-induced error of raindrop distribution measurement using a two-dimensional video disdrometer. J. Atmos. Ocean. Technol. 17, 1483-1492.

Peters, G., Fischer, B., Andersson, T.,2002. Rain observations with a vertically looking micro rain radar (mrr). Boreal Environ. Res. 7, 353-362.

Peters, G., Fischer, B., Munster, H., Clemens, M., Wagner, A.,2005. Profiles of raindrop size distributions as retrieved by microrain radars. J. Appl. Meteorol. 44, 1930-1949.

Petersen, W.A., Rutledge, S.A., 2001. Regional variability in tropical convection: Observations from TRMM. J. Clim. 14, 3566-3586.

Porcù, F., D'Adderio, L.P., Prodi, F., Caracciolo, C., 2013. Effects of altitude on maximum raindrop size and fall velocity as limited by collisional breakup. J. Atmos. Sci. 70, 1129-1134.

Porcù, F., D'Adderio, L.P., Prodi, F., Caracciolo, C., 2014. Rain drop size distribution over the tibetan plateau. Atmos. Res. 150, 21-30.

Radhakrishna, B., Rao, T.N., 2009. Statistical characteristics of multipeak raindrop size distributions at the surface and aloft in different rain regimes. Mon. Weather Rev. 137, 3501-3518.

Ryzhkov, A.V., Giangrande, S.E., Schuur, T.J., 2005. Rainfall estimation with a polarimetric prototype of wsr-88d. J. Appl. Meteorol. 44, 502-515.

Schuur, T.J., Ryzhkov, A.V., Zrnić, D.S., Schönhuber, M., 2001. Drop size distributions measured by a 2D video disdrometer: Comparison with dual-polarization radar data. J. Appl. Meteorol. 40, 1019-1034.

Seliga, T.A., Bringi, V.N.,1976. Potential use of radar differential reflectivity measurements at orthogonal polarizations for measuring precipitation. J. Appl. Meteorol. 15, 69-76.

Sevruk, B., 1982. Method of correction for systematic error in point precipitation measurement for operational use.

Steiner, M., Smith, J.A., Uijlenhoet, R., 2004. A microphysical interpretation of radar reflectivity-rain rate relationships. J. Atmos. Sci. 61, 1114-1131.

Stephens, G.L., L'Ecuyer, T., Forbes, R., Gettelman, A., Golaz, J.-C., Bodas-Salcedo, A., Suzuki, K., Gabriel, P., Haynes, J., 2010. Dreary state of precipitation in global models. J. Geophys. Res.-Atmos. 115.

Tang, Q., Xiao, H., Guo, C.W., Feng, L., 2014. Characteristics of the raindrop size distributions and their retrieved

polarimetric radar parameters in northern and southern China. Atmos. Res. 135, 59-75.

Tao, W.-K., Lang, S., Zeng, X., Li, X., Matsui, T., Mohr, K., Posselt, D., Chern, J., Peters-Lidard, C., Norris, P.M., Kang, I.-S., Choi, I., Hou, A., Lau, K.M., Yang, Y.-M.,2014. The goddard cumulus ensemble model (gce): Improvements and applications for studying precipitation processes. Atmos. Res. 143, 392-424.

Thompson, E.J., Rutledge, S.A., Dolan, B., Thurai, M.,2015. Drop size distributions and radar observations of convective and stratiform rain over the equatorial indian and west pacific oceans. J. Atmos. Sci. 72, 4091-4125.

Thurai, M., Bringi, V.N., 2005. Drop axis ratios from a 2D video disdrometer. J. Atmos. Ocean. Technol. 22, 966-978.

Tokay, A., Bashor, P.G., Habib, E., Kasparis, T., 2008. Raindrop size distribution measurements in tropical cyclones. Mon. Weather Rev. 136, 1669-1685.

Tokay, A., Kruger, A., Krajewski, W.F., 2001. Comparison of drop size distribution measurements by impact and optical disdrometers. J. Appl. Meteorol. 40, 2083-2097.

Tokay, A., Petersen, W.A., Gatlin, P., Wingo, M., 2013. Comparison of raindrop size distribution measurements by collocated disdrometers. J. Atmos. Ocean. Technol. 30, 1672-1690.

Tokay, A., Short, D.A.,1996. Evidence from tropical raindrop spectra of the origin of rain from stratiform versus convective clouds. J. Appl. Meteorol. 35, 355-371.

Ulbrich, C.W., Atlas, D.,1978. The rain parameter diagram - methods and applications. J. Geophys. Res. Ocean. 83, 1319-1325.

Ulbrich, C.W.,1983. Natural variations in the analytical form of the raindrop size distribution. J. Appl. Meteorol. 22, 1764-1775.

Ulbrich, C.W., Atlas, D., 1998. Rainfall microphysics and radar properties: Analysis methods for drop size spectra. J. Appl. Meteorol. 37, 912-923.

Vivekanandan, J., Zhang, G.F., Brandes, E., 2004. Polarimetric radar estimators based on a constrained gamma drop size distribution model. J. Appl. Meteorol. 43, 217-230.

Weisman, M.L., Klemp, J.B., Rotunno, R., 1988. Structure and evolution of numerically simulated squall lines. J. Atmos. Sci. 45, 1990-2013.

Wen, G., Xiao, H., Yang, H.L., Bi, Y.H., Xu, W.J., 2017a. Characteristics of summer and winter precipitation over northern China. Atmos. Res. 197, 390-406.

Wen, J., Zhao, K., Huang, H., Zhou, B.W., Yang, Z.L., Chen, G., Wang, M.J., Wen, L., Dai, H.N., Xu, L.L., Liu, S., Zhang, G.F., Lee, W.C., 2017b. Evolution of microphysical structure of a subtropical squall line observed by a polarimetric radar and a disdrometer during opacc in eastern China. J. Geophys. Res.-Atmos. 122, 8033-8050.

Wen, L., Zhao, K., Chen, G., Wang, M.J., Zhou, B.W., Huang, H., Hu, D.M., Lee, W.C., Hu, H.F., 2018. Drop size distribution characteristics of seven typhoons in China. J. Geophys. Res.-Atmos. 123, 6529-6548.

Wen, L., Zhao, K., Zhang, G.F., Xue, M., Zhou, B.W., Liu, S., Chen, X.C., 2016. Statistical characteristics of raindrop size distributions observed in east China during the asian summer monsoon season using 2D video disdrometer and micro rain radar data. J. Geophys. Res.-Atmos. 121, 2265-2282.

Yang, M., Pan, X., Di, S., 2018. Multi-factor analysis of torrential rain occurred in beijing on July 20, 2016. Journal of China Hydrology. 38, 85-92 (in Chinese).

Yuter, S.E., Houze, R.A.,1995. Three-dimensional kinematic and microphysical evolution of florida cumulonimbus. Part ii: Frequency distributions of vertical velocity, reflectivity, and differential reflectivity. Mon. Weather Rev. 123, 1921-1940.

Yuter, S.E., Kingsmill, D.E., Nance, L.B., Löffler-Mang, M., 2006. Observations of precipitation size and fall

speed characteristics within coexisting rain and wet snow. J. Appl. Meteorol. Climatol. 45, 1450-1464.

Zhang, A., Hu, J., Chen, S., Hu, D., Liang, Z., Huang, C., Xiao, L., Min, C., Li, H., 2019. Statistical characteristics of raindrop size distribution in the monsoon season observed in southern China. Remote Sens. 11, 432..

Zhang, G., Vivekanandan, J., Brandes, E., 2001. A method for estimating rain rate and drop size distribution from polarimetric radar measurements. IEEE Trans. Geosci. Remote Sens. 39, 830-841.

Zhao, S., Sun, J., Lu, R., Fu, S., 2018. Analysis of the 20 July 2016 unusual heavy rainfall in north China and beijing. Meteorological Monthly. 44, 351-360 (in Chinese).